Progress in Surface Science, Vol. 41, pp. 3–49
Printed in the U.S.A. All rights reserved.

0079-6816/92 $15.00 + .00
Copyright © 1992 Pergamon Press Ltd.

ATOMIC FORCE MICROSCOPY

E. MEYER

Institute of Physics, University of Basel, Klingelbergstrasse 82
4056 Basel, Switzerland

Abstract

The basic principles of atomic force microscopy are discussed. Various deflection sensors are described and compared with each other. A simple theoretical basis of the fundamental forces, such as van der Waals, electrostatic, magnetic, capillary, ionic repulsion and frictional forces, is given and the relevant experimental work is summarized.

Contents

Page

1	**Introduction**	5
2	**Basic Principles**	6
3	**Modes of Operation**	7
	3.1 Force vs. Distance Curves	9
4	**Deflection Sensors**	11
	4.1 Electron Tunneling	12
	4.2 Interferometry	13
	4.3 Beam Deflection	14
	4.4 Capacitance Methods	15
	4.5 Comparison between Deflection Sensors	16
5	**Cantilevers**	17
6	**Van der Waals Forces**	18

7	**Electrostatic Forces**	21
8	**Magnetic Forces**	23
9	**Capillary Forces**	26
10	**Ionic Repulsion Forces**	28
11	**Frictional Forces**	33
12	**Elastic and Plastic Deformations**	38
13	**Conclusions**	40
14	**Acknowledgments**	42
	References	42

Abbreviations

AES	auger electron spectroscopy
AFM	atomic force microscopy
CE	contact electrification
CD	corona discharge
DFM	dipping force microscope
EFM	electrostatic force microsope
FM	frequency modulation
FFM	friction force microscope
JKR	Johnson-Kendall-Roberts
LB	Langmuir-Blodgett
LEED	low-energy electron diffraction
LFM	lateral force microscope
MFM	magnetic force microscope
PMMA	polymethylmethacrylate
PSD	position sensitive detector
RHEED	reverse high energy electron diffraction
SEM	scanning electron microscope
SEMPA	scanning electron microscope with polarization analysis
SFA	surface force apparatus
SPM	scanning probe microscope
STM	scanning tunneling microscope
UHV	ultra high vacuum
XPS	x-ray photoelectron spectroscopy

1 Introduction

The scanning tunneling microscopy (STM) has already become a useful tool in surface science in its ability to characterize surfaces of metals and semiconductors in real space on an atomic scale [1, 2]. One of the main limitations of STM is the requirement of sample conductivity. In 1986 Gerd Binnig, Calvin Quate and Christoph Gerber [3, 4] proposed a new type of microscope which could overcome this limitation. Instead of measuring tunneling currents between a probing tip and sample, the authors suggested measuring forces on an atomic scale. The atomic force microscope (AFM) is a synthesis of the mechanical profilometer, using mechanical springs to sense forces, and the STM, using piezoelectric transducers for scanning. One year after this first publication, Binnig and coworkers [5] presented the first atomic resolution on graphite. In the same year Albrecht *et al.* [6] obtained atomic resolution for the first time on an insulator, boron nitride. After these milestones in the history of AFM the development continued at a high pace. Insulators, such as photosensitive silver halides, could be characterized by AFM without exposure to radiation. Organic materials, such as fragile Langmuir-Blodgett films, could be imaged from microns down to the molecular scale. Biological macromolecules, polymers, ceramics and glasses are other examples investigated by AFM. Apart from being applied to different materials, the instrument was improved continuously. New detection methods, microfabricating processes for the sensor preparation and incorporation of the microscope into different environments, such as liquids, vacuum, and low temperature, are examples of the various modifications the instrument has undergone.

The basic principle of this microscope to measure forces or to measure interactions between a sharp probing tip and sample surface led to the creation of a variety of other scanning probe microscopes (SPM), such as the magnetic force microscope (MFM), the dipping force microscope (DFM), the friction force microscope (FFM), and the electrostatic force microsope (EFM). By these new developments the field became further subdivided. Concurrently, there is also an unifying tendency to combine different methods such as STM/AFM, AFM/MFM, AFM/FFM. This provides the unique opportunity to characterize a single nm-sized spot by a combination of methods and therefore gain more information than by the separate application of a single method. The same development evolved some years ago in electron spectroscopy, where different methods, such as Auger electron spectroscopy (AES), x-ray photoelectron spectroscopy (XPS) and low-energy electron diffraction (LEED) were combined in one single chamber. Nowadays, this has become a standard in commercial ultra high vacuum (UHV) chambers. Some of the UHV analytical chambers have already incorporated STM's and the addition of AFM and other SPM's can be foreseen.

The development of commercial microscopes followed the pace of research. AFM and STM are the most succesful instruments in the field of SPM. The possibility to apply AFM to conductive as well as to insulating materials has attracted not only surface physicists and chemists but also biologists, physicians, electrochemists, and mechanical engineers. Commercial AFM's can be applied routinely with an efficiency comparable to electron microscopes. Samples are measured without special surface preparation at ambient pressure or in liquids. The instrument characterizes the morphology of the samples with quantitative information about properties such as roughness or height distributions.

The layout of this article is as follows. First, more detailed descriptions of the basic principles, modes of operation and instrumentation are given. Then emphasis is placed on different forces which can be sensed by AFM; their origins, some simple theoretical descriptions and the corresponding applications. The subdivision of forces into sections is not always unambigous, especially in the case of repulsive contact imaging where most of the forces, such as van der Waals, electrostatic, capillary forces, ionic repulsion or frictional forces, can contribute simultaneously and their separation is difficult. Some examples are given where a separation of several contributions is achieved, e.g., magnetic and van der Waals or frictional forces and ionic repulsion forces.

2 Basic Principles

In force microscopy the probing tip is attached to a cantilever-type spring. In response to the force between tip and sample the cantilever, also called lever, is deflected. Images are taken by scanning the sample relative to the probing tip and digitizing the deflection of the lever or the z-movement of the piezo as a function of the lateral position x, y. Typical spring constants are between 0.001 to 100N/m and motions from microns to ≈0.1Å are measured by the deflection sensor (cf. Fig. 1). Typical forces between probing tip and sample range from 10^{-11} to 10^{-6}N. For comparison the interaction between two covalently bonded atoms is of the order of 10^{-9}N at separations of ≈Å. Therefore, non-destructive imaging is possible with these small forces. Two force regimes are distinguished: Contact and non-contact mode. When the microscope is operated in non-contact mode at tip-sample separations of 10 to 100nm, forces, such as van der Waals, electrostatic, magnetic or capillary forces, can be sensed and give information about surface topography, distributions of charges, magnetic domain wall structure or liquid film distribution. At smaller separations of the order of Å the probing tip is in contact with the sample. In this mode, ionic repulsion forces allow the surface topography to be traced with high resolution. Under best conditions atomic resolution is achieved. In addition, frictional forces and elastic or plastic deformations can be detected under appropriate conditions.

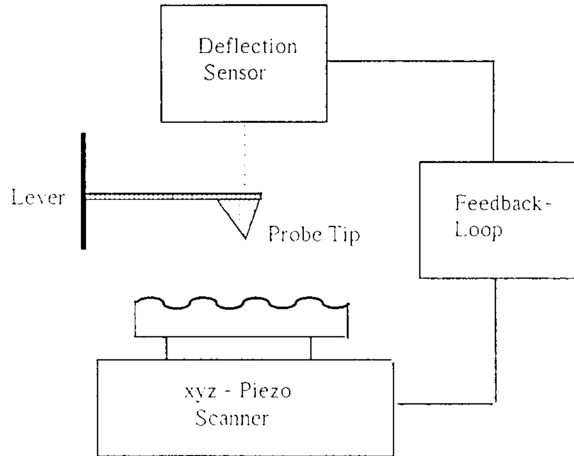

Figure 1:
Basic principle of AFM. A sharp probing tip is mounted on a cantilever-type spring. The force between tip and sample causes cantilever deflections which are monitored by a deflection sensor. While scanning the sample a feedback-loop can keep the deflection constant (equiforce mode).

3 Modes of Operation

First, we have to distinguish between static modes, also called dc-modes, and dynamic modes, also called ac-modes. In the *static mode*, the cantilever-type spring bends in response to the force F which acts on the probing tip until the static equilibrium is established. As derived from Hooke's law, the deflection z_t of a cantilever is proportional to the force $F = c_B z_t$ where the proportional constant is the spring constant c_B. A beam with constant cross section has a spring constant which is given by

$c_B = 3EI/l^3$

where E is the Young's modulus, l the length and I the moment of inertia. For a rectangular beam of width b and thickness d the moment of inertia I is given by

$I = bd^3/12$.

With the dimensions $1 \times 10 \times 100 \mu m^3$ of a rectangular Si-cantilever ($E=1.69 \cdot 10^{11} N/m^2$) a spring constant of c_B=0.42N/m is derived. In the static, mode typical forces between 10^{-10} to 10^{-6}N are measured.

While scanning the surface the deflection can be kept constant by regulating the height of the sample relative to the probing tip. This mode, called *equiforce mode*,

is the most common mode. The height profiles of a homogeneous sample (neglecting variations of elasticity...), measured with van der Waals or repulsive ionic forces, are interpreted as topography. As an alternative the height position of the sample is kept constant and the variations of the lever deflection are digitized. This mode, called *variable deflection mode*, allows high scanning speeds. For atomic scale imaging this mode is quite common, because the height variations are small on this limited area. Thus, the interpretation is similar to the equiforce mode.

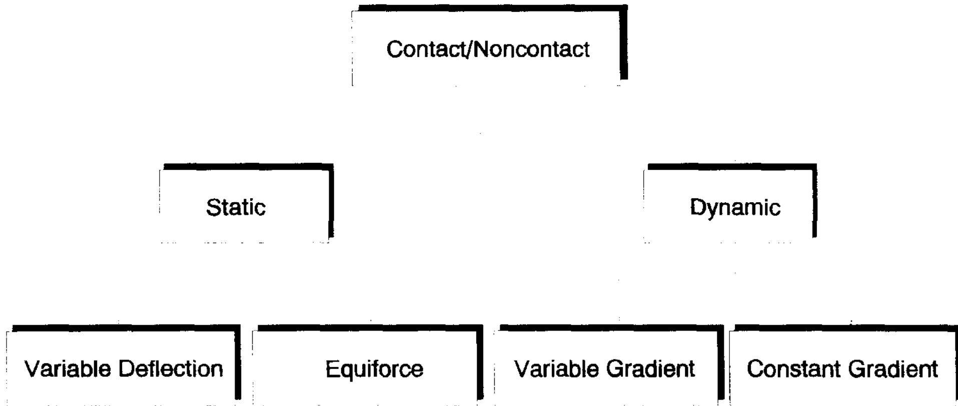

Figure 2:
Possible modes of operation.

In the *dynamic mode* the lever is oscillating close to its resonance frequency. A distance-dependent force $F(z)$ shifts the resonance curve. The equation of motion of the rectangular beam is given by

$$\frac{\partial \Psi^4}{\partial x^4} + \mu/EI \frac{\partial \Psi^2}{\partial x^2} = F(x,z)$$

where $\mu = m/l$ is the mass density. With the Ansatz $\Psi = Y(x)T(t)$ the differential equation can be separated. The time dependent part is described by a harmonic equation $T + \omega^2 T = 0$. The nth Eigenfrequency is given by

$$f_n = \frac{(\kappa_n l)^2}{2\pi l^2}\sqrt{\frac{EI}{\mu}} = \frac{(\kappa_n l)^2}{2\sqrt{3}\pi}\sqrt{\frac{c_B}{m}} \tag{1}$$

where $f_n = 2\pi\omega_n$ and κ_n depends on the space dependent part and therefore also depends on the force acting on the tip. For the above mentioned Si-cantilever the resonance frequency of the first Eigenmode is found to be 138 kHz ($\rho{=}\mu/(c \cdot d){=}2.33{\cdot}10^3$kg/m^3, $\kappa_1 l{=}1.875104$).

In first approximation only the force gradient $F' = \partial F/\partial z$ influences the resonance frequency. An effective spring constant is defined by

$c_{eff} = c_B - F'$.

A repulsive force ($F' < 0$) stabilizes the spring and increases the resonance frequency, whereas an attractive force destabilizes the spring and lowers the resonance frequency

$$f_1 \approx 0.32\sqrt{\frac{c_{eff}}{m}} = 0.32\sqrt{\frac{c_B - F'}{m}}$$

In the ac-mode the feedback loop either asserts constant amplitude (slope detection) or keeps the frequency constant (FM-detection) [7]. Both methods have the same physical content: The resonance curve is fixed to a certain position during the whole scan and profiles of *constant gradient* are measured. As an alternative the feedback loop is disabled and *variable gradient* images are acquired. Again, the constant gradient images are easier to interpret, whereas the variable gradient mode allows higher scan speeds. In the ac-mode, force gradients between 10^{-5} and 10^1 N/m are measured. With a simple force law of the form $F(z) = const \cdot z^{-n}$ the corresponding forces at a distance of $z{=}10$nm range between between 10^{-13} to 10^{-7}N.

3.1 Force vs. Distance Curves

In contrast to the above described modes, the acquisition of force vs. distance curves does not involve a change of lateral position but measures the force as a function of distance between probing tip and sample. Usually, the deflection z_l is monitored as a function of sample position z_s. By multiplying the deflection z_l with the spring constant c_B the net force F_{lever} is derived. For non-contact measurements F_{lever} is equal to the attractive force, F_{attr}, between tip and sample. In the contact mode long-range attractive and short-range repulsive forces F_{rep} are equilibrated by the elastic deformation of the lever : $F_{lever} = F_{attr} + F_{rep}$. The repulsive force which acts on the contact zone is not derived unambigously. Some assumptions about the tip radius and decay lengths of attractive and repulsive forces have to be made.

In first approximation, neglecting elastic deformations, the distance between probing tip and sample, z, is derived from $\Delta z = \Delta(z_l - z_s)$. Thus, the force vs.distance curve $F_{lever}(z_s)$ yields the desired force law $F_{lever}(z)$. With the above mentioned restrictions $F_{rep}(z)$ and $F_{attr}(z)$ can be determined. The reverse direction, when a model potential is presumed and the corresponding force vs. distance curve is derived, is shown in Fig. 3.

The instabilities occur at the points where the derivative of the force equals the spring constant. A more sophisticated model is the Johnson-Kendall-Roberts (JKR) model which includes both adhesive forces and elastic deformations [8]. This model has been already applied to surface force apparatus (SFA) measurements. In SFA-experiments the calculations are completely analogous to the AFM and the reader is referred to the SFA-literature [9].

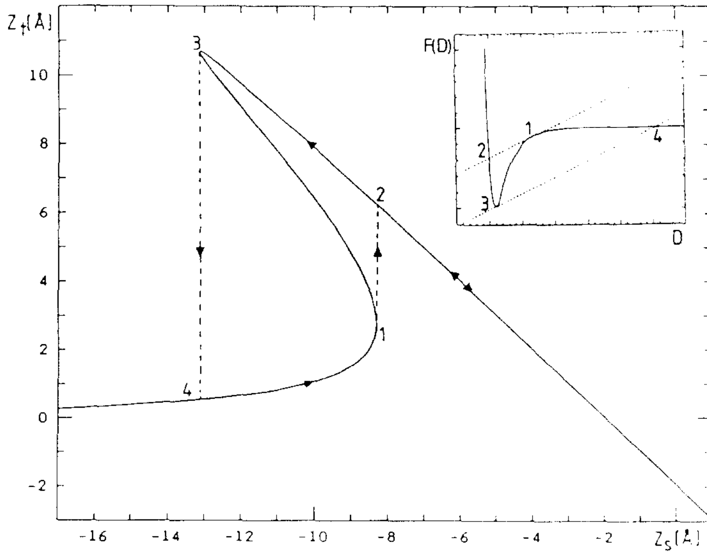

Figure 3:
Force vs. distance curve from a Lennard-Jones-type potential as shown in the inset. At points 1-2 and 3-4 the force derivative equals the spring constant and instabilities occur. For details see [11].

Instead of measuring the force as a function of z-distance, force gradients can be monitored in the ac-mode. This method is more accurate, especially for non-contact measurements. After the acquisition of the force gradient vs. distance curve the force is derived by numerical integration. Pethica et al. [10] suggested that ac-measurements should also be used for contact meausurement where the local stiffness can be determined. A combination of dc- and ac-measurements allows the determination of the complete set of parameters of the JKR-model.

4 Deflection Sensors

The first deflection sensor was based on electron tunneling [3]. The resolution of the sensor was found to be sufficient to achieve atomic resolution [3, 6, 11, 12]. However, tunneling is rather sensitive to contaminants and the interaction between the tunneling tip and the rear side of the lever can become comparable to the interaction between probing tip and sample. Therefore, other techniques, such as optical interferometry, laser beam deflection and capacitance methods have been introduced. In contrast to tunneling, these deflection sensors are far away from the lever at distances of microns to centimeters. For the optical techniques the interaction is given by the light pressure which is of the order 10^{-12}N. For the capacitance method electrostatic forces can influence the performance but are typically below 10^{-11}N. Thus, the interaction forces betweeen these sensors and the cantilever are negligible for most applications. On the other hand, the miniaturization of the optical methods is limited by the wavelength of light, which might be of importance in finding the ultimate limits of force microscopy.

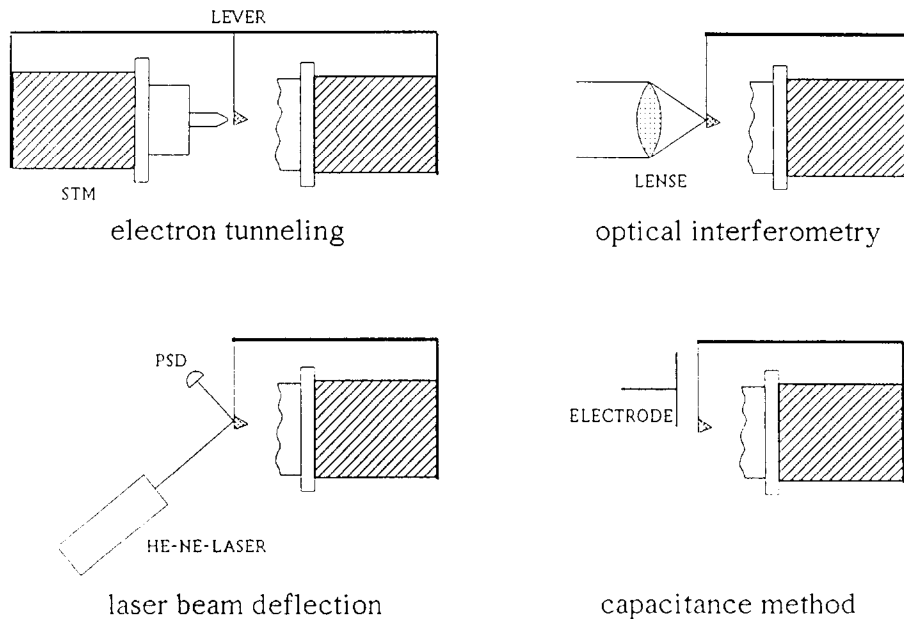

Figure 4:
Several force microscope designs. In each set-up, the sample piezo is shown on the right, the cantilever in the middle, and the corresponding deflection sensor is indicated on the left.

For low temperature experiments the laser power of 1-1000μW, used for optical methods, is a point which favours tunneling where the electrical power, dissipated on the rear of the lever, is reduced to the order of a few nW. In the following section the basic concepts, the sensitivities and the limitations are described for each detection technique.

4.1 Electron Tunneling

Electron tunneling originates from the overlap of wavefunctions between the tip and surface atoms. The tunneling current between two metals is given by

$I = I_0 \cdot \exp(-A\sqrt{\Phi}z)$

where A=1.025eV$^{-1/2}$Å^{-1}, Φ is the barrier height and z the distance between the electrodes [1]. For typical barrier heights of 4eV, the tunneling current decays one order of magnitude when the distance z is increased 1Å. Therefore, the tunneling tip is at close proximity to the sample, typically at distances of 5-10Å. In order to calculate the sensitivity of tunneling, a small modulation Δz is applied. The relative variations of the tunneling current are then given by

$\Delta I/I = 1 - \exp(-A\sqrt{\Phi}z) \approx A\sqrt{\Phi}z \approx \sqrt{\Phi}z$

where Δz is in Å and Φ in eV. A distance modulation of 0.1Å causes a current variation of 20% which shows that tunneling is a very sensitive method allowing distances as small as 0.01Å to be measured. However, typical tunneling currents are of the order of nA requiring high amplifications which limit the bandwidth to a few kHz. In the dynamic mode the lever is oscillating at its resonance frequency which is typically 30-100kHz for microfabricated cantilevers. Therefore, most of the applications are performed in the static mode. Another handicap of the tunneling detection method is its sensitivity to contaminants such as oxides or hydrocarbons. The presence of contaminants causes the tip to press on the lever until the nominal tunneling current is achieved. Forces as high as 10^{-6}N have been reported under these conditions [14, 15]. For ideal tunneling between metals, the forces are reduced to 10^{-9}N [16]. Empirically, it is found that freshly evaporated gold films and PtIr-tips are necessary to achieve stable tunneling conditions at ambient pressure [11]. For standard applications in air the tunneling method is too delicate and optical methods are more reliable and easier to operate. For UHV and low temperature experiments the low power of nW and the possibility to minimize the dimensions seem to be advantageous. First succesful low temperature AFM experiments in high vacuum [17] and UHV [18] have clearly demonstrated that the tunneling detector is well-suited to these conditions.

4.2 Interferometry

Interferometric deflection sensors have the intrinsic advantage that the length scale is given by the wavelength of the laser and all calibrations of piezos are easily done. The measured photocurrent is proportional to the light intensity I which is given by the superposition of the object beam and the reference beam:

$I = |\vec{E}_O^2 + \vec{E}_R^2| = I_O + I_R + \sqrt{I_O I_R}\cos(\Phi)$

where Φ is the phase difference between the electric fields $\vec{E}_O$, $\vec{E}_R$ of object and reference beam, and I_O,I_R are the corresponding intensities. The phase difference depends on the difference between the optical path of the reference and object beam:

$$\Phi = \Phi_0 + \frac{4\pi\Delta z}{\lambda}$$

where λ is the the wavelength and Δz the deflection of the lever. For maximum sensitivity the phase difference is shifted by piezoelectric positioning to $\Phi_0 = m\pi/2$ where m is an integer.

Then, the relative variations of the intensity are approximately given by

$$\frac{\Delta I}{I} = \frac{2\sqrt{I_O I_R}(\frac{4\Pi\Delta z}{\lambda})}{I_O + I_R}$$

which can be reduced to

$$\frac{\Delta I}{I} = \frac{4\pi\Delta z}{\lambda} \approx \frac{\Delta z}{\lambda}$$

for $I_O \approx I_R$. A modulation of Δz=0.1Å causes a relative intensity variation of 10^{-5} which is 4 orders of magnitude less than in electron tunneling. However, typical photocurrents are μA to mA where only small amplifications are required for the current voltage converter. With a stable interferometer and low-noise electronics these small variations can be measured and spectral sensitivities of 10^{-4}Å$/\sqrt{Hz}$ can be measured and the bandwidth can be increased to 100kHz or MHz. Good dynamic mode performance has been reported by several groups using homodyne [19, 20] or heterodyne interferometry [21]. Good performance in the static mode crucially depends on the rigidity and compactness of the design. In addition, spurious reflections should be avoided in order to achieve a good low-frequency stability.

Small phase differences between the object and reference beam turned out to be useful for the optimization of the signal-to-noise ratio. In the fiber-optic based design by Rugar *et al.* [22] the reference beam is the beam reflected by the cleaved end of a fiber which is mounted a few microns away from the lever. An elegant design has been developed by Sarid et al. [23]. The cantilever is placed in front of a laser diode

facet. A fraction of the laser light is reflected into the laser diode. This optical feedback causes variations of the laser intensity which are proportional to the phase between reflected and emitted beam and, therefore, are a measure of the deflection of the lever. Another design by Schönenberger *et al.* [24, 25] uses a common-path interferometer where the two polarisation directions serve as reference and object beams. Similar concepts can be applied to the heterodyne interferometers [26]. The limitations of the optical methods are given by shot noise: $I_S = \sqrt{2eIB}$ where e is the elementary charge and B the bandwidth. For a bandwidth of 100kHz, a wavelength of 780nm and I=1μA, a minimum deflection of Δz=1.8Å is calculated. For frequencies above a few kHz, detectors are found to be shot noise limited. For lower frequencies other noise sources, such as 1/f or Johnson noise of the electronics limit the sensitivity. For most practical purposes the shot noise limit is negligible compared to the thermal noise of the cantilever. Only in the contact mode where thermal vibrations are reduced drastically is the resolution limited by the detector. Interferometric detection is well-established for the dynamic mode. In combination with high-Q cantilevers and FM-detectors, the highest sensitivities can be achieved [7].

The rather high laser power (μW to mW) and the limitation of miniaturization by the wavelength of light are the disadvantages of optical interferometry which have to be taken into account for special applications.

4.3 Beam Deflection

This optical method is based on a simple concept that turns out to be very appropriate for force microscopy [27, 28]. A laser beam is reflected off the rear side of the cantilever. In the early days of force microscopy small mirrors were mounted on the cantilever. Nowadays, the surface of the microfabricated lever is smooth enough to be used as mirror. The position of the reflected beam is monitored by a position sensitive detector (PSD), a two- or four-segmented photodiode. The difference between intensity from the upper and lower halfes of the diode divided by the total intensity gives a direct measure of the deflection of the lever:

$$\frac{\Delta I}{I} = \frac{I_A - I_B}{I_A + I_B} = \frac{6\Delta z}{l}\frac{1}{\delta}$$

where l is the length of the lever and δ the beam divergence of the reflected beam. This angle is determined either by the focuse length f and aperture D of the lenses : $\delta \approx D/f$ or by the diffraction on the lever: $\delta \approx 2\lambda/b$ where b is the width of the cantilever. For typical cantilever dimensions of the order of 10μm the reflected beam is found to be diffraction limited. Therefore, the relative variation of the photocurrent is given by

$$\frac{\Delta I}{I} = \frac{3\Delta z}{l}\frac{b}{\lambda} \approx \frac{\Delta z}{\lambda}$$

where the approximation is valid for $l \approx 3b$. This result shows the close similarity between interferometry and beam deflection. Both methods are limited by the wavelength of light and have similar sensitivities. Due to the simplicity of beam deflection very compact and rigid designs can be constructed. The standard resolution in the static mode is 0.1Å. Most of the commercial instruments are based on beam deflection and are designed for repulsive contact imaging. For dynamic mode imaging results comparable to interferometry detection can be achieved [29]. The method depends on a good reflectivity of the lever, which excludes the application of wires in practice. It is a great advantage that beam deflection can be easily extended to a bidirectional force sensor. Instead of the two-segment photodiode, a quadrant diode is used. Then, the difference between left and right half of the photo diode (C-D) is proportional to the torsion of the cantilever [30, 31], which is proportional to the lateral force acting on the probing tip. Force microscopes where both the lateral and the normal forces are measured are called friction force microscopes (FFM), and will be discussed later.

4.4 Capacitance Methods

Capacitance methods are less comon than optical methods. However, their potential sensitivity makes them attractive for future developments. The capacitance of a plate capacitor is given by $C = \varepsilon_r \varepsilon_0 A/z$, A the area of the plate, z the distance between the plates. Therefore, a small change of distance will cause a change of the capacitance and a change of the voltage:

$$\frac{\Delta U}{U} = \frac{\Delta z}{z}.$$

At a mean distance z=1μm, a change of Δz=0.1Å causes a relative variation of 10^{-5} which is comparable to the optical methods. Several set-ups, such as the capacitor bridge or the resonant phase shift, have been introduced [32, 33, 34]. Displacements as small as 0.1Å are measured. Dielectric breakthrough was found to limit the applied voltages to tens of volts. Furthermore, the electrostatic force gradient can cause the "snap-in" of soft cantilevers to the capacitor plate. The whole detector plus cantilever can be built by microfabrication. The integration appears to be simpler than in the case of optical methods where relatively complicated devices, such as laser diodes or fibers, are needed. For ultra-small instruments at low temperature, this design might be a promising alternative.

4.5 Comparison between Deflection Sensors

	$\frac{\Delta I}{I}$	$\frac{\Delta I}{I}$ (Δz=0.1Å)	I	displacements
Tunneling	$\sqrt{\Phi}\Delta z$	0.2	nA	10^{-2}Å[3]
Beam Deflection	$\Delta z/\lambda$	10^{-5}	μA-mA	10^{-4}Å/ $\sqrt{Hz}$[27]
Interferometry	$\Delta z/\lambda$	10^{-5}	μA-mA	10^{-4}Å/ $\sqrt{Hz}$[22]
Capacitance	$\Delta z/z$	10^{-5}	Volts	10^{-1}Å[32]

	+	-
Tunneling	very sensitive good dc-stability	forces from tunneling tip delicate preparation limited bandwidth roughness of lever thermal drift
Beam deflection	easy to operate small interaction	reflectivity of mirror (no wires) diffraction limited high laser power fluctuations of beam divergence
Interferometry	any shape of lever large bandwidth intrinsic length scale	diffraction limited high laser power spurious reflections
Capacitance	good sensitivity microfabrication	interaction between electrodes (lever instabilities) dielectric breakthrough

5 Cantilevers

In order to be sensitive to small forces the spring constant c_B has to be selected as small as possible (0.01-100N/m). On the other hand, the influence of acoustic waves and building vibrations should be minimized and the resonance frequency has to be kept high ($\approx$ 10-100kHz). According to equation (1) the resonance frequency is proportional to $\sqrt{c_B/m}$. Therefore, the mass of the cantilever has to be minimized which means that the dimensions should be minimized, too. Typical dimensions of thickness, width and length are $1\times10\times100\mu m^3$ which gives for a Si-lever a resonance frequency of 138kHz and a spring constant of 0.42N/m.

The basic limitations in resolution for the non-contact mode are given by thermal vibrations. The amplitude of the first Eigenmode $\langle\psi\rangle$ is given by $\langle\psi\rangle^2 \approx k_BT/c_B$ which yields 0.15Å for our example. When the probing tip interacts with the sample, the spring constant c_B is substituted by the effective spring constant c_{eff}. Therefore, the thermal vibrations increase in the attractive regime and decrease in the repulsive regime. The spring constant should also be above 1-10N/m. Otherwise, the lever snaps into contact at large separations.

In the contact mode the thermal vibrations of the cantilever become negligible. Here, adhesion forces in the z-direction and frictional forces in the lateral direction have to equilibrated by the lever. Typical spring constants for repulsive contact imaging are between 0.01 to 1N/m. With softer springs the probing tip sticks to the surface and cannot be moved anymore. Only on surfaces with small frictional forces and reasonably small adhesion, spring constants as small as 0.001N/m can be used (e.g. Langmuir-Blodgett films).

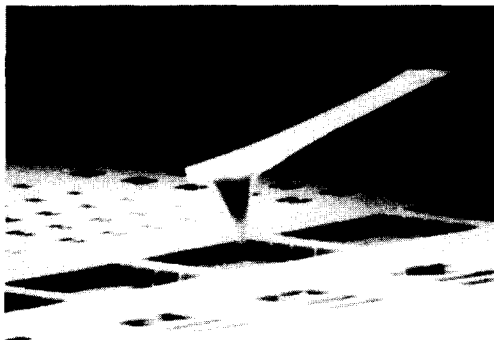

Figure 5:
SEM-image of a microfabricated Si-cantilever positioned above a test sample. By courtesy of O. Wolter (from [35]).

There exist many preparation procedures for cantilevers. Thin metallic wires are etched and bent towards the sample. Foils can be cut in stripes and small pieces of, e.g., diamond are glued to the cantilever. These methods are all very time consuming and need a lot of manual skill. Therefore, batch fabrication has become very common. The microfabrication processes are based on well-known integrated circuit process technology. With photolithography the silicon-wafer is patterned. With wet and dry etching certain faces of the silicon are etched preferentially. Thin films of SiO_2 or Si_3N_4 can be deposited in addition. Due to high precision alignment, accuracies of 0.1μm are achieved, allowing the sensor fabrication with good reproducibility. The cantilevers usually have integrated tips made of silicon [35, 36], SiO_2 or Si_3N_4 [37]. Typical radii of curvature of the tips are 10 to 30nm. These levers are now commercially available. Manufacturer also offer a variety of geometries which are optimized to particular applications, e.g. hard levers for non-contact mode, softer levers for contact-mode, conductive levers for combined STM/AFM, magnetic tips with high aspect ratio for MFM, or levers with small lateral spring constant for FFM.

6 Van der Waals Forces

Van der Waals forces are present in all force microscope experiments. They arise from the instantaneous polarization of atoms which interact with surrounding atoms. The classical London equation [38] describes the interaction energy between two nonpolar molecules:

$$V_n(z) = -\frac{3}{4}\frac{\alpha^2 h\nu}{(4\pi\varepsilon_0)^2 z^6} = -\frac{C_n}{z^6}$$

where α is the polarizability, ν a characteristic absorption frequency (for transparent materials typically in the UV-regime), ε_0 the dielectric constant and h Planck's constant. The dependence on the polarizability α indicates that van der Waals forces can be anisotropic, because the polarizability along or perpendicular to a moleculr axis can be different. This anisotropy has some interesting consequences for the spatial arrangement of liquid crystals and polymers and might also be of interest for future AFM experiments.

For distances larger than 20nm, retardation effects become dominant. Casimir and Polder [39] show that at distances larger than $\lambda = c/\nu$, the interaction energy between two atoms is approximately described by

$$V_r(z) = -\frac{23hc\alpha^2}{8\pi^2(4\pi\varepsilon_0)^2 z^7} = -\frac{C_r}{z^7}$$

If we assume that van der Waals forces are additive, the nonretarded force of a sphere, representing an AFM probing tip (typically R = 10-100nm radius of curvature), above a plane, representing the sample, is approximately given by

$F_n = -AR/z^2$

where A is the Hamaker constant. For the retarded case

$F_r = 2\pi BR/(3z^3)$

can be derived, where B is the retarded van der Waals constant. The constants A and B are related to the microscopic constants C_n,C_r by simple relations $A = \pi C_n \rho^2$ and $B = 0.1\pi\rho^2 C_r$ where ρ is number of molecules per m^3 [44]. However, the assumption of additivity is not fulfilled. Manybody interactions have to be taken into account.

A correct microscopic description is rather complicated. As an alternative, the Lifshitz theory treats manybody effects correctly, but treats the interacting particles as a continuum [40]. Within this macroscopic theory the power-law dependence of distance is found to be in aggreement with the results found by simple integration. Only the Hamaker constants have to be determined and this is done from the dielectric constants of spherical tip (ε_1), immersion medium (ε_2) and planar sample (ε_3). Neglecting contributions from the lower frequencies (static and infrared) the Hamaker constant is given by

$$A \approx h\nu_e \frac{(n_1^2 - n_3^2)(n_2^2 - n_3^2)}{f(n_1, n_2, n_3)}$$

where $n_i = \sqrt{\varepsilon_i}$ are the refractive indices at the absorption frequency ν, typically at $3{\cdot}10^{15}$Hz and $f(n_1, n_2, n_3)$ has a positive value [9]. From the above formula can be seen that van der Waals forces can be either attractive or repulsive. The repulsive forces arise only when a medium is immersed between two different materials and when the condition $n_1 \leq n_2 \leq n_3$ is fulfilled. For identical materials in both probing tip and sample, the van der Waals forces are always attractive.

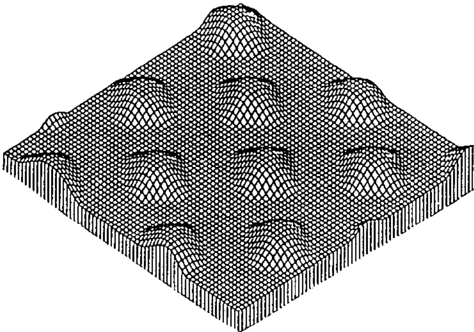

Figure 6:
AFM measurement performed in the non-contact mode. A silicon test pattern (200nm periodicity) is imaged with a sharp probing tip (radius of curvature 20nm). Besides van der Waals force, electrostatic and capillary forces can also influence the measurements. Courtesy of M. Nonnenmacher (from [45]).

A more detailed treatment of the theoretical aspects of van der Waals forces in relation to force microscopy is given by Hartmann, including retarded forces and different

immersion media [41]. Some estimations of the van der Waals forces are made by Goodman and Garcia [42]. For a typical tip radius of R=100nm at a distance of z = 1nm, forces between 1 to 20nN are found. E.g., graphite tip on graphite sample gives 8nN, diamond on mica 17nN, and SiO_2 on graphite 1.2nN.

The measurement of van der Waals forces has a long tradition which started years before the invention of the atomic force microscope. Derjaguin and Abrikosova [43] measured the forces between a hemisphere and a flat surface of polished quartz at distances of 100-1000nm. They found good agreement to the calculated retarded forces. Tabor and Winterton [44] observed both regimes of retarded and nonretarded forces using the surface force apparatus (SFA). Here, the forces between sheets of atomically smooth mica were measured at close separations of 5 to 30nm. At about 10nm the transition from retarded to nonretarded forces was observed. The SFA measurements were performed systematically under different conditions (immersed liquids, gases and vapors, deposited Langmuir-Blodgett films) [9].

The force microscopy measurements, performed in the van der Waals regime, are still rare and rather preliminary. Martin et al. [21] measured attractive forces between a tungsten tip on a silicon surface at ambient conditions. The measurements were performed in the ac-mode with a heterodyne interferometer as deflection sensor. Force gradients of 0.01N/m to 2N/m and corresponding forces (determined by integration) between 10^{-11}N to $1.5 \cdot 10^{-9}$N were found at distances of 3nm to 18nm. Van der Waals forces were also used to image surfaces, such as silicon, graphite, photoresists, and proteins [21, 45]. The highest lateral resolution was 50Å. Moiseev et al. [46] reported the dependence of lateral resolution as a function of distance which was found to be in agreement to their theoretical analysis. Hartmann [41] presented force vs. distance curves measured by a capacitive sensor. For distances larger than 40nm agreement with the model of retarded forces was found. For smaller distances some deviations from the theoretical predictions were found which were attributed to contaminants being present at ambient conditions. Ducker et al. [29] performed ac-force measurements between a Ni-tip and mica. They observed not only the typical shift of the resonance curve with smaller distance but also a decrease of the Q-factor. The origin of this dissipative force is still uncertain. A possible explanation might be the theoretically predicted van der Waals friction [47].

For future experiments well-defined conditions, either ultra high vacuum or immersion in liquids, are required. Another issue to be discussed is the geometry of typical probing tips which deviates from simple geometries and makes a theoretical treatment difficult. As an alternative, specially designed cantilevers with spherical apex could be used for AFM experiments. It would also be of great interest to find the ultimate resolution limits of force microscopes operated in the van der Waals regime. The achievement of atomic resolution appears questionable but is also a real challenge.

7 Electrostatic Forces

The distribution of charges on surfaces is of both scientific and industrial interest. Charges can be deposited either by contact electrification (CE), also called triboelectrification, or by corona discharge (CD). Different objects, such as toner particles in electrophotography, ice particles in clouds, shoes on carpets, electrical switches, and CD-treated polymer foils depend crucially on charge transfer. The mechanisms of the charge transfer in metal-metal, insulator-metal, and insulator-insulator contacts are poorly understood. Electronic band structure, specific surface sites (e.g. kinks) or ionic conductivity may influence the electron transfer during electrification. With force microscopy surface charge distribution can be measured with unprecedented high resolution. Ultimately, single electrons are detectable.

The force between a conductive tip and a charge distribution on an insulating film is given by

$F_{charge} = q_t E_z$

where q_t is the induced charge on the tip and E_z the electrical field. The induced charge has two contributions:

$q_t = -(q_s + C \cdot V)$

where q_s is induced on the tip by the surface charge distribution and the term $C \cdot V$ originates from the voltage, V, between the tip and back electrode with capacitance C. In addition to F_{charge}, called 'charge' force, the 'capacitive' force gives a further contribution which is given by

$$F_{capacity} = 1/2 \frac{\partial(CV^2)}{\partial z} = 1/2 V^2 C'$$

where C is the capacitance between the electrodes and $C' = \partial C / \partial z$ the derivative of the capacitance. The total force is then described by the sum of 'charge' and 'capacitive' force

$$F_{total} = q_t E_z + 1/2 C' V^2 = -(q_s + C \cdot V) E_z + 1/2 C' V^2 \qquad (2)$$

In a first approximation, E_z is proportional to the charge on the sample. Therefore, the first two terms are a measure of the charge distribution. By changing the polarity, the 'charge' force signal reverses its sign and can be easily distinguished from other forces, such as van der Waals forces or magnetic forces. When the voltage is modulated, $V = V_0 + V_1 \sin \omega t$, the 'capacitive' contribution can even be measured separately at 2ω, whereas the 'charge' force is found as a dc-signal and a signal at ω.

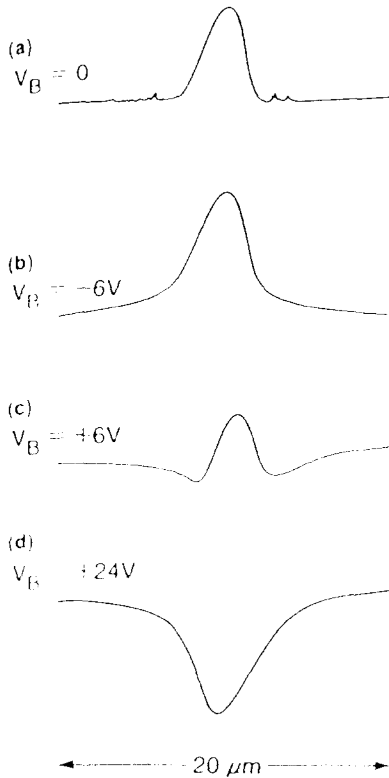

Figure 7:
Contours of constant force gradient of a negative charge deposited on PMMA by applying a voltage of 100V at a distance of ≈1000Å. The contrast is reversed by changing the polarity which demonstrates that electrostatic forces dominate. Courtesy of B. Terris (from [50]).

For a spherical tip of radius R above a flat sample, the 'capacitive' force is roughly given by

$F_{capacity} = -\pi\varepsilon_0 RV^2/z_{eff}$

where z_{eff} is the effective distance between tip and sample. $z_{eff} = z_0 + h/\varepsilon$ depends on the thickness h of the insulating film with dielectric constant ε. The 'capacitive' force is independent of the surface charge, but can be used to measure local variations of the dielectric constant or to estimate the tip radius R. The above equation is only a good approximation for $z \leq R$. For typical measurements at $z \geq$ 10nm and $R \approx$ 10-20nm, a slower z-dependence $z^{-\alpha}$ is observed [48] with α between 0.3 to 0.6 rather than $\alpha = 1$. The capacitive force has been extensively used in the field of MFM. Here, this electrostatic force is superimposed on the magnetic forces in order to provide a constant background, which is necessary to prevent tip crashes.

The 'charge' forces have been used for characterization in a variety of experiments where surface charges are involved. The first observation by Stern et al. [49] was an example of corona discharge. Localized surface charges were deposited by applying a voltage pulse of $\approx 500V$. Afterwards, the charges were imaged in the constant gradient

mode. The charge could be easily distinguished from topography by varying the voltage. By changing the polarity a reversal of the contrast was observed, which corresponds well to the linear voltage dependence of the 'charge' force in equation (2). Decay rates of the charge peak on polymethylmethacrylate (PMMA) and sapphire were found to be faster than observed on a macroscopic scale. The origin of this difference is not yet understood.

A further improvement was achieved by Schönenberger and Alvarado [48]. Small amounts of charge were deposited on Si_3N_4 by voltage pulses of $\approx$ 10V. Within a few seconds, the 'charge' force decayed in a staircase fashion. The steps correspond to the recombination of single charge carriers. From the decay rates it is concluded that the electrons move via thermionic emission. At distances of $\geq$ 20nm and voltages of 2-6 V, tunneling and field emission are negligible.

A study of contact electrification has been performed by Terris et al. [50]. On silicon surfaces, bombarded by 0.3μm polystyrene spheres, charged regions as small as 0.2μm were found. On PMMA and polycarbonate charges were deposited by touching the tip to the surface. The charge transfer to the surface was found to depend on the applied voltage, but was independent of the number of contacts and the contact time. For macrosopic contacts, it is known that the transferred charge increases with the number of contacts. It was suggested that subsequent contacts have different contact areas and therefore increase the amount of charge. In contrast, this mechanism can be ruled out in force microscopy. With the high accuracy of positioning by force microscopy, the same area is charged several times. Hence, the discrepancy between macroscopic and microscopic observations is well understood and helps to reveal the origins of contact electrification.

Another example of imaging surfaces with electrostatic forces has been performed by Saurenbach et al. [51]. The polarization charges of ferroelectric materials cause a 'charge' force on the tip. Thus, the domain wall in a sample of ferroelectric $Gd_2(MoO_4)_3$ could be observed by force microscopy.

The investigation of electrostatic forces is just beginning. Some refinements, such as implementation in vacuum, should allow a more systematic study. To observe single electrons or to measure currents as small as 10^{-19}A are exemplary oppurtunities for future fundamental studies with the EFM.

8 Magnetic Forces

Force microscopes which are specially dedicated to magnetic forces are called magnetic force microscopes (MFM). Up to now about 50 publications have appeared, giving a good impression of the intensive research in this field. A complete description of these results goes beyond the scope of this review and the reader is referred to some excellent reviews about MFM [52, 53, 54].

The investigation of magnetic microstructure is important for the understanding of surface magnetism. Domain wall formation not only depends on spin-dependent band structure but also on features such as grain boundaries, impurities and surface morphology. On the technological side, magnetic storage media are of great interest. Optimization procedures are sought in order to improve storage density.

In order to be sensitive to magnetic forces, the probing tip is made of ferromagnetic materials, such as Ni, Fe or Co. The stray field of the sample, H, causes a force on the tip which is evaluated by integrating over the tip volume

$$F_m = \int_{tip} \nabla_r(\vec{M}(\vec{r}\,') \cdot \vec{H}(\vec{r} + \vec{r}\,')dV' \qquad (3)$$

where $\vec{M}$ is the magnetization of the tip. Two special cases are illustrative: (1) The tip is approximated by a magnetic dipole $\vec{m}$ which results in a force

$$F_m = \vec{m} \cdot \nabla \vec{H}.$$

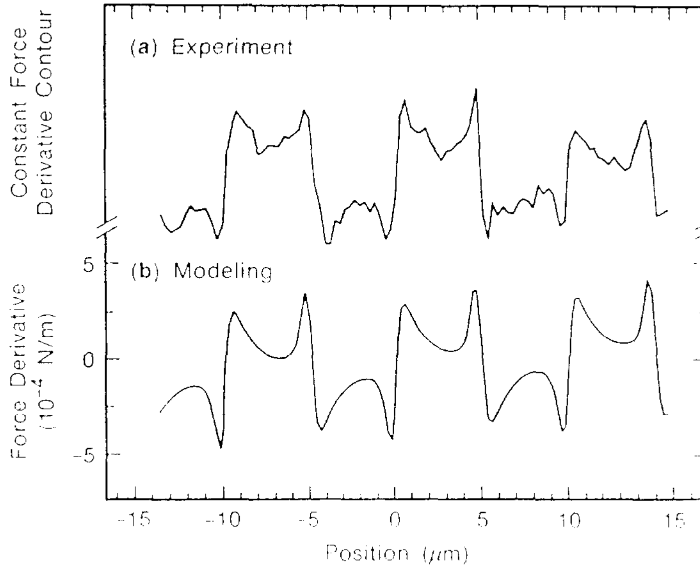

Figure 8:
(a) Contours of constant force gradient of bits of a magnetic recording media. (b) Corresponding model calculation. Courtesy of D. Rugar (from [55]).

Therefore, one expects to probe the derivative of the stray field in the equiforce mode and the second derivative in the constant gradient mode. Experimentally, good

agreement is found with the dipole approximation when the dipole is not positioned on the tip apex but within the probing tip [55]. (2) With a very long tip domain, only one pole contributes significantly to the force. In this single-pole approximation, the force is given by

$$F_m = m \cdot H_z$$

where m is the dipole moment per unit length of the tip. In this case, equiforce images give a direct measure of the stray field and constant gradient images are related to the first derivative of the stray field. For certain tip geometries a better agreement to the experimental results was found with the single-pole approximation [54].

The above equations are only rough estimates. In order to get more quantitative results numerical or analytical integration of equation (3) has to be performed. One has also to take into account that either tip or sample magnetization can be distorted by the harder magnetic material. Wall motion and reversal of magnetization were reported with soft materials.

Most of the first MFM experiments were performed on technological samples, such as magneto-optical recording media or longitudinal recording media. These magnetic materials have large stray fields which makes them well suited to be characterized by MFM. Compared to other methods such as Kerr microscopy, Lorentz microscopy, scanning electron microscopy with polarization analysis (SEMPA), electron holography or Bittern technique the main advantage of MFM lies in its simplicity in handling without requiring any sample preparation. Advanced digital data acquisition allows routine measurements.

Soft magnetic materials such as Permalloy (NiFe) or Fe whiskers are more difficult to be imaged and the stray field of the tip can cause wall distortion and wall motion. Some improvement could be made by the use of microfabricated levers with thin magnetic coatings which reduces the stray field significantly and allows practically distortion-free imaging of soft magnetic materials, such as Permalloy [53].

A quantitative interpretation of the data is rather involved. At present, experimental results could be reproduced by simulations with reasonable accuracy. In most cases the domain wall thickness was then assumed to be infinitely small. A determination of the sample magnetization out of the experimental data can not be done unequivocally. The observed lateral resolution is typically 100nm and could be improved in special cases to 10nm. A further improvement appears to be difficult but still appears possible. At low temperatures the stray field of superconductors can be sensed by MFM [56]. Here, the main purpuse is to image vortices and to compare the measurements with calculations based on the Ginzburg-Landau theory. The simultaneous measurement of magnetic contrast and of topography appears to be one of the most promising aspects. First experiments which clearly demonstrate this capability have been reported already [54].

9 Capillary Forces

AFM measurements performed under ambient conditions, are influenced by the presence of vapors, in particular by water vapor. Either the surfaces are already covered by thin films or liquid condenses between probing tip and sample. In both cases a meniscus is formed which strongly draws the tip towards the sample. The interaction is dominated by the Laplace pressure which is described by

$P = \gamma(1/r_1 + 1/r_2) = \gamma/r_K$

where γ is the surface tension, r_1, r_2 are the radii of the meniscus and r_K the Kelvin radius. The force is then derived by multiplying the Laplace pressure by the contact area of the meniscus, A:

$$F_{Capillary} = \frac{\gamma A}{r_K} = \frac{\gamma 2\pi R d}{r_K}$$

where R is the tip radius and d the tip penetration depth into the liquid. A rough estimate of the maximum capillary force is given by $F_{max} \approx 4\pi R\gamma$.

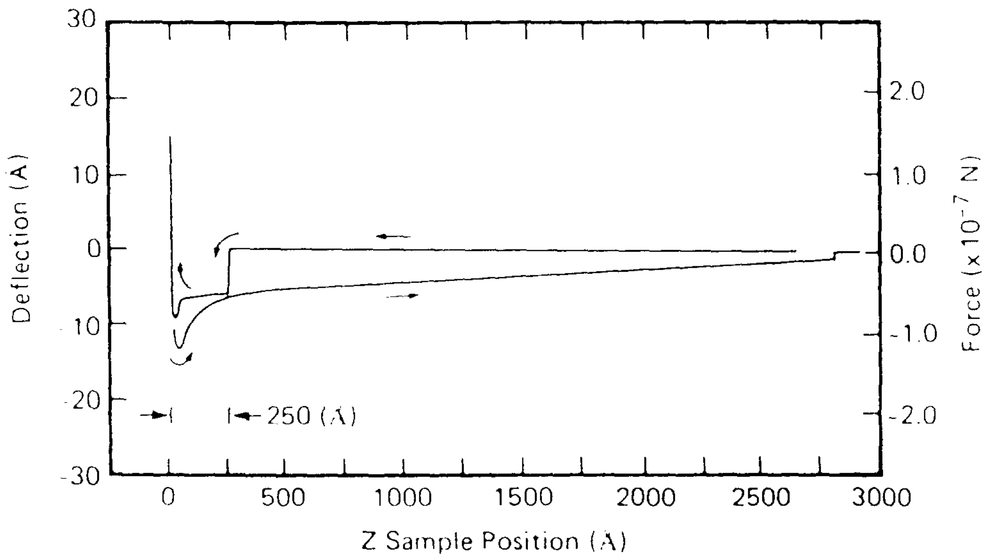

Figure 9:
Force vs. distance curve on a perfluoropolyether polymer liquid film. On approach, the tip first contacts the liquid surface and a meniscus is formed. On continued approach, the force remains constant until the tip reaches the substrate, where ionic repulsion forces take over. On retraction of the tip a pull-off force of $1.2 \cdot 10^{-7}$N is needed to break the meniscus. Courtesy of M. Mate (from [58]).

For a typical tip radius of $R = 100$nm and $\gamma = 70$mN/m a force of 90nN is calculated which is large compared to typical van der Waals forces of 1-10nN. These large forces can have drastic effects on the contrast mechanism of repulsive contact imaging. The forces in the contact region can become so large that the outermost tip atoms are removed. As a consequence, single atom imaging is not possible anymore and multiple tip imaging occurs. The large forces can also cause plastic deformation on very soft samples. The question arises of how these capillary force can be avoided. Weisenhorn et al. suggest immersing the tip and sample completely into liquid [57]. Small forces of 1nN are reported with measurements in water, related to the elimination of capillary forces. The measurements in liquids are not trivial at all. E.g., the interaction of hydrocarbons in water is much stronger than in vacuum or air. The origin of this additional force is related to the hydrophobic effect, where water molecules rearrange around the hydrocarbons in order to optimize the network of hydrogen bonds. This increase of local order is related to a local decrease of entropy and causes the additional forces. Another way to circumvent the presence of capillary forces is to incorporate the instrument in vacuum chamber or a chamber with dry nitrogen.

Besides these negative aspects of capillary forces, which disturb the imaging conditions, they can be used to characterize thin films. Force vs. distance provide the first instability on approach, where the tip is attracted by the liquid. The tip then advances through the liquid until the solid surface is reached and repulsive forces take over. The distance between these points determines the thickness of the film. Alternatively, the liquid surface can be imaged in the noncontact mode. Afterwards, the solid substrate can be imaged with repulsive forces. A substraction of the two images yields the distribution of the film.

Mate et al. performed a systematic study on thin polymeric fluorocarbon films on silicon and on magnetic storage media [58, 59]. The distribution of these films is of interest for technological applications because they are used as lubricants. A detailed comparison between AFM measurements and ellipsometry data revealed a systematic offset in film thickness derived by AFM. This offset probably originates from an additional liquid film on the probing tip which causes an increase in the measured film thickness. Other explanations might involve van der Waals forces between probing tip and liquid film which cause a distortion on the liquid film or molecules which extend over the mean liquid surface. A combined study of AFM, ellipsometry and XPS demonstrated that the fluorocarbons lie flat on top of the surface with film thicknesses of 15 to 25Å which is smaller than the radii of gyration between 32 to 73Å (molar weights are between 5000 to 26000) [60]. Measurements of the disjoining pressure showed high values of up to 5 MPa. Therefore, entropic effects become less pronounced and the conformation

is determined mainly by the strong attraction of the molecules to the substrate which explains the small film thickness.

Questions about the fluidity of thin films were adressed by Burnham et al. [61] and Blackman et al. [62]. From force vs.distance curves, Blackman et al. could distinguish three cases: liquid-like behaviour for unbound perfluoropolyether, solid-like behaviour for Langmuir-Blodgett films of cadmium arachidate, and intermediate for bonded perfluoropolyether. These AFM measurements actually show that the classical concept of liquid vs. solid breaks down at these small dimensions. Different approaches have to be found to describe these systems in a more adequate way.

10 Ionic Repulsion Forces

In the previous section, long-range forces are treated. Here, we describe the forces which arise when probing tip and sample are in contact.

For soft springs, there is a sharp transition between contact and non-contact. At the point where the gradient of the long-range forces equals the spring constant, an instability occurs and the lever snaps into contact. For van der Waals forces and a spring constant of 0.1N/m, this instability occurs at a distance z of $\approx$10nm where $\frac{\partial F}{\partial z} = A \cdot R/z^2$=0.1N/m, A is the Hamaker constant, and R=100nm is the approximate tip radius. For capillary forces the instability occurs when the liquid surfaces are in close proximity. In contact, the long range forces are still present and sum up over a rather large region of the tip (the diameter of this region is related to the range of the interaction). The attractive forces have to be equilibrated by the repulsive forces, causing large local stress on the tip and sample and can cause damage. By retracting the sample, a part of the attractive forces can be compensated by the lever deflection. Close to the second instability, where the lever snaps back, the forces acting on the contact region are minimized. The above description is the most common case in repulsive contact measurements. An alternative approach is to use hard spring constants of $\approx$100N/m in combination with sharp probing tips, which minimize attractive forces; this arrangement can circumvent the instability and a continuous transition from the attractive to the repulsive contact region is observed.

Ionic repulsion forces originate from the Pauli exclusion principle which prevents electrons from occupying states with the same quantum numbers, and from Coulombic repulsion between nuclei which can arise from incomplete screening at these small distances. These repulsive forces are extremely short ranged and decay within tenths of an angstrom. Hard sphere models, power laws of the form $v(z) = (\sigma/z)^n$, $n \geq 9$, and exponential potentials $v(z) = C \exp(-z/\sigma)$ are in reasonable agreement to experimental data, such as helium scattering. However, a physical derivation of these potentials is lacking. In close analogy to van der Waals forces, the equiforce scan lines are interpreted

as topography of the sample. In comparison to the non-contact van der Waals imaging, the contact measurements have achieved higher lateral resolution. The interpretation of these high resolution images is rather difficult and requires complex quantum mechanical calculations that treat the system of probing tip and sample as an entirety. *Ab initio* calculations based on quantum mechanical Kohn-Sham equations [63, 64] and molecular dynamics based on empirical potentials that include many-body terms [65] have been adapted to the case of AFM. For a detailed description of these theoretical treatments, the reader is referred to the original literature. Conclusions which can be drawn out of these calculations are briefly summarized below:

The equiforce images are loosely interpreted as contours of constant total charge density. Repulsion forces should be limited to 10^{-9} to 10^{-10}N; otherwise, bonds are broken and single atom imaging is not possible anymore [66, 64]. Not only the repulsion of atoms is found but also weak bonds (physisorption) are predicted [64]. For metallic tips on metallic samples, strong metallic adhesion is found which can lead to wetting of the tip and destruction of the sample and/or tip [67]. For the case of layered materials, a continuum theory has been combined with *ab initio* calculations [68]. The observation of local elasticity by AFM is predicted, as well as an upper limit of forces before destruction starts. Finally, some theoretical papers clearly show that not only normal forces [65, 69] are operative but also lateral forces can arise, described in more detail in the next section.

The amount of experimental work in the field of repulsive contact imaging is huge and can be found in different areas, such as biology, physics, chemistry or metrology. Therefore, a complete summary is not intended and the reader is referred to some recent reviews which cover part of this work [4]. In the following section we will restrict discussion to some selected applications that demonstrate the resolution capabilities of the microscope. The first applications of AFM were dedicated to the atomic resolution of samples such as graphite [3, 11, 12, 13], mica [20], boron nitride [6] and transition metal dichalcogenides [70, 71]. In all these experiments the atomic lattice was observed and lattice spacings in agreement to the bulk values were found. On these layered materials rather high forces of up to 10^{-7}N could be applied and still atomic-scale features were observed which demonstrates that these features do not necessarily require a monatomic tip but that the contact region can be as large as several hundred atoms. The atomic-scale features likely arise from a certain degree of commensurability between sample and tip and are often closely related to frictional forces.

The fact that the first applications were restricted to layered materials led also to the suggestion that layers of the sample are sheared against each other which should yield the observed contrast [10]. In the next stage of AFM studies, ionic crystals were resolved on an atomic scale. The easy shear plane of these crystals is not coincident with the image plane and therefore the shearing mechanism could be ruled out in these

experiments. Alkali halides, such as NaCl [72] and LiF [73], and silverhalides, such as AgBr [74] were investigated and square lattices of 2.8Å, 4.0Åand 4.1Å, respectively, were observed. The distances between protrusions were found to be in agreement with the spacing between equally charged ions. From a comparison of ionic radii, it was concluded that the probing tip predominantly senses the larger anions leaving the smaller cations undetected [75]. Only in the case of KBr where the ionic radii of anion and cation are comparable could both ions be imaged [18]. In some cases aperiodic features such as steps or point defects could be resolved on an atomic scale. On KBr, monatomic steps were found which were resolved on an atomic scale [18].

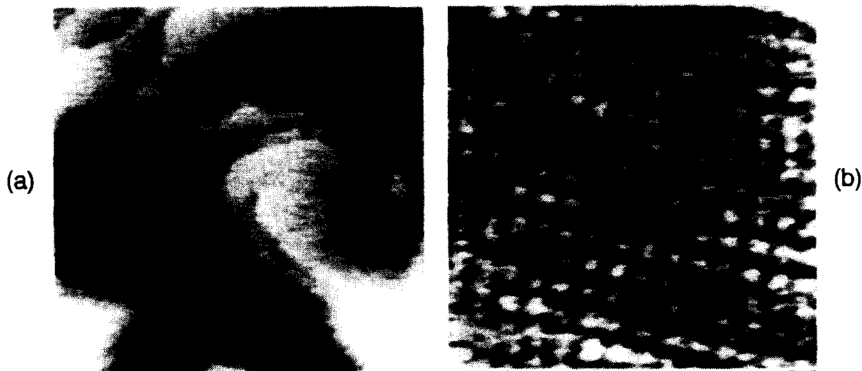

Figure 10:
AFM measurement on AgBr(001) performed in the contact mode. (a) Monatomic steps can be seen and a screw dislocation emerges in the middle of the image ($500\times500nm^2$) (b) High resolution image. The protrusions are separated by 0.41nm and are attributed to the bromine ions (from [74]).

The ability of AFM to image single point defects is still controversial. Experiments on organic systems such as Langmuir-Blodgett films [76] and polymers [77] have reported isolated molecular defects and isolated molecules. The quality of the data is still lower than the best atomic resolution of defects observed by STM. Reasons for these limitations might be: (1) Probing tips which are typically less sharp than the electrochemically etched STM metal tips. (2) Long range forces, such as capillary and van der Waals forces, which increase the stress in the repulsive contact region. (3) Contaminations, which are present in most of the experiments which were performed under ambient conditions.

Experiments which are performed under well-defined conditions, such as UHV, on

highly detailed structures, such as Si(111)7×7, will hopefully yield clear statements about the resolution limits of contact imaging. Nevertheless, AFM has already demonstrated itself to be extremely useful by giving accurate results on the nm-scale.

In the next section, we focus our attention on some selected applications that provide information difficult to obtain by other surface sensitive techniques.

Silver halides have unique properties that render them indispensable for the photographic process. Despite a financial interest in replacing expensive silver, no alternatives have been found. The surface properties of silver halides in particular play an important role in the formation of the latent image. Charged kink sites and jogs are believed to attract photoelectrons and silver interstitials, forming silver clusters.

Figure 11:
AFM measurement of a photographical emulsion ($12\times12\mu m^2$). Triangular and hexagonal tabular grains are visible. The picture is illuminated from the right side. Courtesy of U.Schwarz (from [82]).

Investigations by conventional techniques, such as RHEED or LEED, are hindered by charging effects, beam damage and photolysis. Only noble metal decoration has yielded information about the step structure of silver halides. However, this method is limited to a lateral resolution of 50-100Å and provides practically no quantitative information in the z-direction. AFM offers the oppurtunity of imaging these surfaces without radiation exposure , a drawback of some of the conventional analytical methods. Fig. 10 shows an AFM image of AgBr(001) where steps of monatomic height (2.9Å) are resolved [74]. In the center of the growth hill a screw dislocation emerges. The AFM results confirm some results of the decoration technique, such as step structure and orientation, and yield new results, such as step heights, screw dislocations and enhanced resolution in regions of high step density. On the terraces atomic resolution is achieved with a lattice spacing of 4.1Å. These measurements support an unreconstructed 1×1 surface. As mentioned before, only one atomic species, the larger bromide ions, is observed. Measurements on AgBr(111) showed both the atomic lattice of 4.2Å and a superstructure of 60Å [78]. The superstructure is probably related to a reconstruction of the surface, previously observed by the decoration technique. More detailed AFM experiments in UHV may

render more exacting details of the surface reconstruction. Similar studies of inorganic crystals are performed on fluorides, such as CaF_2, BaF_2, and SrF_2. Cleavage faces [80] and epitaxially grown films [79] are characterized by AFM.

Further experiments on AgBr have shown that the surface is rather mobile and easily deformable. By increasing the force and applying a small z-modulation to the tip small holes can be drilled into the surface. On a time scale of minutes these holes are refilled again by the rapid diffusion of silver and bromide ions. From these measurements the surface diffusion coefficient is estimated to be $9 \cdot 10^{-14} cm^2/sec$ which is about 3-4 orders of magnitude larger than the diffusion coefficient of gold [81]. This high ionic mobility is one of the key properties in the formation of the latent image.

The study of the surfaces of single crystals and epitaxially grown films of AgBr has been extended to photographic emulsions. Micrometer-sized tabular grains (T-grains) have been characterized by AFM [82]. In this study some fine details, such as nm-sized growth hills and the superstructure on the (111)-facets are resolved. Some limitations of the technique are encountered as well. The steep side-walls of T-grains and some details on top of the T-grains can not be imaged correctly due to the convolution between surface and tip geometry that originates from the limited aspect ratio of the probing tip.

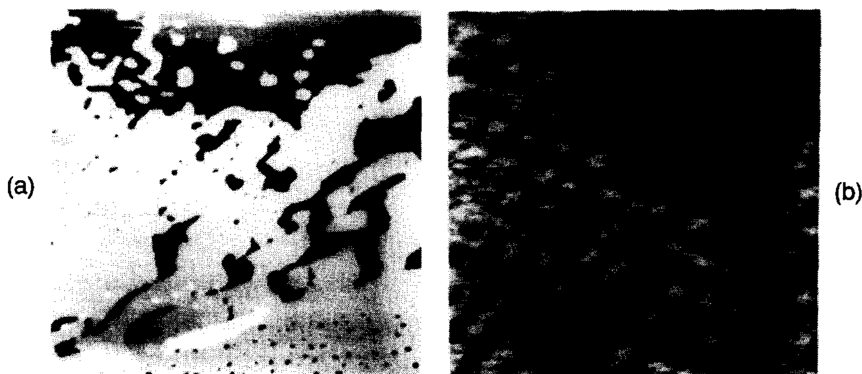

Figure 12:
(a) AFM image of a $3500 \times 3500 nm^2$ area of a 4-layer Cd-arachidate film. Steps of bilayer height are visible (from [81]).(b) $5.3 \times 5.1 nm^2$ area of a 4-layer Cd-arachidate film. The spacing between the protrusions is about 0.5nm which correponds well to the intermolecular distances (from [85]).

Generally, rough surfaces with large gradients and features with high aspect ratio are rather difficult to image by scanning probe microscopes [83]. Careful analysis of the experimental data and optimization of the tip geometry are required to exclude tip artifacts and to achieve credible images of these surfaces.

Another class of materials that are amenable to AFM imaging are ultra-thin organic films, such as Langmuir-Blodgett (LB) films. In close analogy to the silver halides, the organic films are easily destroyed by an electron beam. Therefore, studies with methods such as LEED [84] are rare and rather difficult to be performed. The films are fragile and AFM has to be performed with forces below $\approx 10^{-8}$N. Fortunately, the air-exposed surface of most of the films is hydrophobic and practically free of a water film. Therefore, AFM-measurements at ambient pressure become possible and are not disturbed by capillary forces. In the topography mode, molecular resolution has been achieved on films of Cd-arachidate showing a lattice of approximately 5Å spacing [85]. Furthermore, some molecular defects and step structure has been observed [76]. In the meantime, AFM has become an established technique for the characterization of LB-films, allowing optimization of transfer conditions. Fundamental questions such as phase transitions or phase separation of mixed films [101] can now be adressed.

A number of AFM studies on organic crystals [87, 88] have been performed where properties such as lattice parameters or step structure were determined. In certain cases even deviations from the bulk-terminated surfaces were found [89], indicating that a reconstruction is energetically more favorable. Biological materials have been studied in great detail and the reader is again referred to other reviews [90].

11 Frictional Forces

When the probing tip slides along the surface, frictional forces can arise. In comparison to macroscopic friction experiments, use of AFM to measure friction has some significant advantages: The contact is reduced to essentially one single asperity; The sliding is performed under controlled force, speed and direction; and the normal forces and lateral forces can be measured simultaneously and are compared from point to point. On the other hand, there are also some restrictions: At present the exact contact zone is not well known and the tip geometry is not completely controlled. Therefore, the technique is not very accurate to give absolute numbers but is extremely sensitive to find relative variations on a local scale.

Microscopes with the capability of measuring both topography and friction channels simultaneously, but separately, are called friction force microscopes (FFM) or lateral force microscopes (LFM). Usually the measurements are performed in the equiforce mode, regulating with constant normal force, and the lateral forces are digitized. Two different designs have been introduced:

(1) Two separate deflection sensors are positioned perpendicular to each other. The two signals give a direct measure of the lateral and normal deflections of the cantilever. Cantilevers with quadratic or spherical cross sections are best suited for this method. As deflection sensors, optical interferometry [91], capacitance methods [32] and electron tunneling [93] have been implemented.

(2) Laser beam deflection can be easily adapted to measure both bending and torsion of the cantilever [30, 31]. As a position sensitive detector, a four segment photo diode is used. The difference between the signal from upper and lower segments (A-B) is proportional to bending, i.e., to normal forces, whereas the difference between the signal from the left and right segments (C-D) is proportional to torsion, i.e., to lateral forces. The torsion spring constant for a rectangular cantilever is given by

$$c_t = \frac{Gbd^3}{3lr^2}$$

where G is the shear modulus, d the thickness, r the length of the tip and l the length of the cantilever. Maximum torsion is achieved with rather long cantilevers with long tips and small thickness.

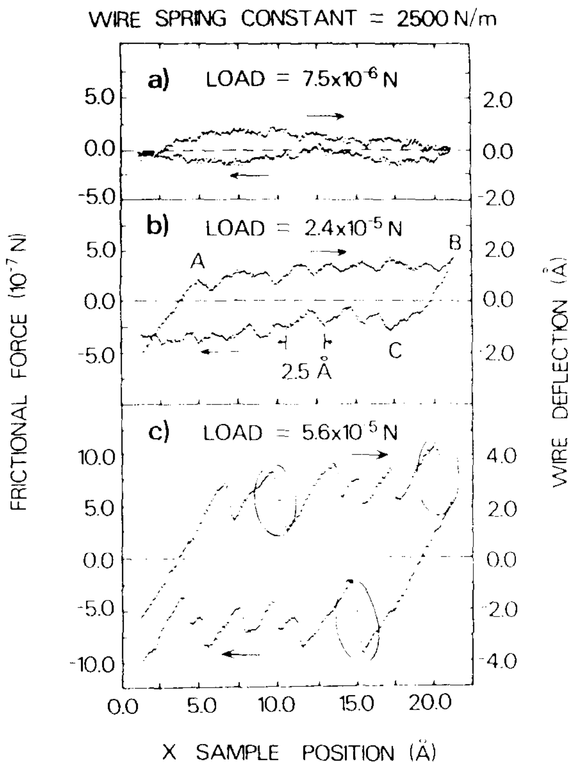

Figure 13:
Frictional force between a tungsten tip and a graphite surface as a function of sample position for three different loads. The circled parts in (c) indicate double slips. Courtesy of M. Mate (from [95]).

Typically, normal forces between 10^{-7} to 10^{-9}N and frictional forces between 10^{-6} to 10^{-10}N are measured. With specially designed Si-cantilevers having normal spring constants of 0.001N/m and torsion spring constants of 1-0.1N/m, lateral forces as small as 10^{-11}N can be measured [101]. However, these levers are limited to surfaces with low surface energy. Otherwise, they stick to the surface and regular scanning is not possible anymore.

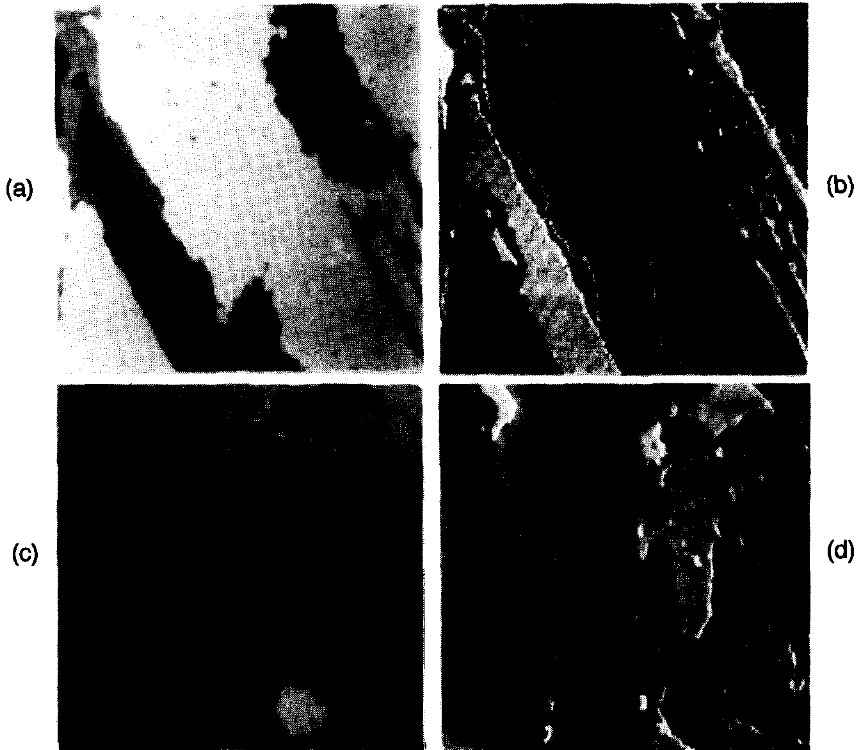

Figure 14:
FFM measurements on Langmuir-Blodgett films. On the left the topography is displayed and on the right the friction force map.
(a) Double bilayer film of Cd-arachidate (2×2μm) showing bilayer steps. (b) Corresponding friction force map showing increased friction on the substrate compared to the organic film.
(c) Bilayer film of Cd-arachidate (2×2μm). (d) Corresponding friction force map. An arrowhead-shaped structure is observable. The structure is interpreted as a material inhomogenity (from [98]).

The origins of friction on a microscopic scale are poorly understood. Phonons or electronic excitations are likely created by a sequence of instabilities. Either tip or surface atoms are moved out of their equilibrium positions until an instability occurs. Then, the stored elastic energy is released in a short time and dissipative processes can occur. Recently it also has been shown that the spring constant can have significant influence on the size of the frictional forces [94]. For soft cantilevers the instability occurs not at the tip-surface interface, but the spring itself is unstable. The instabilites arise when the derivative of the lateral force equals the lateral spring constant or torsion spring constant. In close analogy to the instabilities which occur in the force vs. distance curve in the normal direction, the lever jumps at these critical points. The hysteresis causes a scan-direction dependence. Within this model, friction does not only depend on the properties of the contacting surfaces and the applied load, but also on the spring constant. For hard springs, reduced friction is expected, whereas soft springs yield maximum friction. As mentioned in the section "Ionic Repulsion Forces", some quantum mechanical calculations have been performed for systems such as a Pd-tip on graphite [69] and silicon on silicon [65]. The molecular dynamics calculations appear to particularly suitable for treating rather large systems of up to a few thousand atoms [92] offering the possibility of simulating AFM experiments.

The first observation of friction with a force microscope showed that lateral forces between a tungsten tip and graphite vary with the atomic periodicity of the underlying graphite surface [95]. The lateral forces were found to be proportional to the load and a low friction force coefficient of 0.01 was determined. The onset of atomic-scale stick slip was observed at $2 \cdot 10^{-6}$N for a 155N/m spring and $5 \cdot 10^{-5}$N for a 250N/m spring, demonstrating that the stick slip originates from instabilities of the cantilever. Loads of up to 10^{-4}N were applied and still atomic scale features were observed. At these high loads single atom imaging can be excluded. The contact diameter was estimated to be $\approx$100Å and the atomic scale features were related to a certain degree of commensurability between tip and sample. Similar results were found on other layered materilas such as mica [20] and MoS_2 [96].

Technological applications have been demonstrated by Kaneko et al. [97]. They characterized magnetic discs by measuring topography, friction and local adhesion. They found characteristic differences between lubricated and unlubricated discs.

Further progress was made by incorporating the FFM into ultra high vacuum (UHV). G. Meyer and N. Amer [31] demonstrated simultaneous measurements of friction and topography on NaCl(100). They found increased lateral forces on scanning up an atomic step. Energies of up to 50eV were deposited by traversing such a step. The exact origin of this dissipative process at steps is unknown. Neubauer et al. [32] measured friction loops as a function of load with an iridium tip on gold. They found a strong hysteresis

of friction on loading and unloading. On loading a friction coefficient of 1.0 is found while on unloading it is 0.4. This hysteresis was related to a change of the tip-surface interface, e.g. rearrangement of atoms or formation of new bonds.

An alternate way for doing well characterized tribological experiments is to investigate multilayers of Langmuir-Blodgett films. Single and double bilayer of Cd-arachidate have been investigated by FFM [98, 99]. With forces below 10nN, wearless friction is observed. Fig. 14a/b shows a $2 \times 2 \mu m^2$ scan area where three different regions can be distinguished: the lowest level in topography corresponds to the substrate, the intermediate level is one bilayer above the substrate and the high level corresponds to two bilayers. On the film covered regions the frictional forces are found to be ten times smaller than on the substrate. This observation clearly demonstrates that the Langmuir-Blodgett films act as lubricants on a microscopic scale. Between the first and second bilayer only minor differences in friction are found. Only on the bilayer films some inhomogenieties are observed which are related to local variations of the material composition. (cf. Fig. 14c/d) Interestingly, these inhomogenieties are observed only in the friction force map but not in the topography.

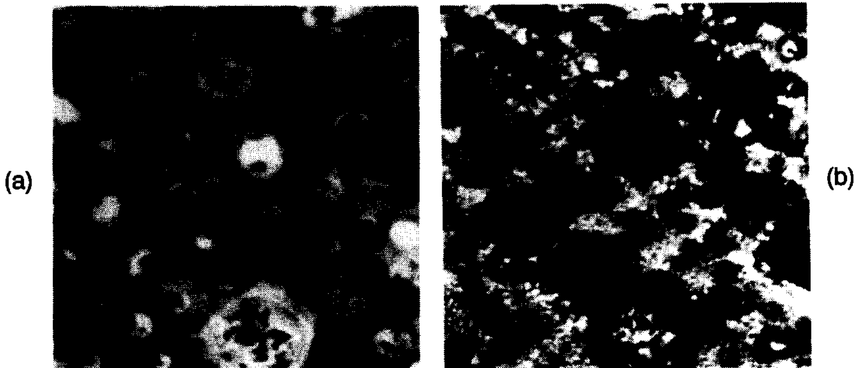

Figure 15:
(a) Topography of a LB-bilayer prepared from a mixture of fluorocarbon and hydrocarbon carboxylates. The circular domains are assigned to the hydrocarbon component and the surrounding flat film to the fluorinated component ($5 \times 5 \mu m$). Holes in the hydrocarbon islands are 5nm deep and reveal the substrate.
(b) The friction force map indicates low friction on the hydrocarbons, intermediate on the fluorocarbons and highest friction on the silicon substrate. Courtesy of R. Overney. (from [100]).

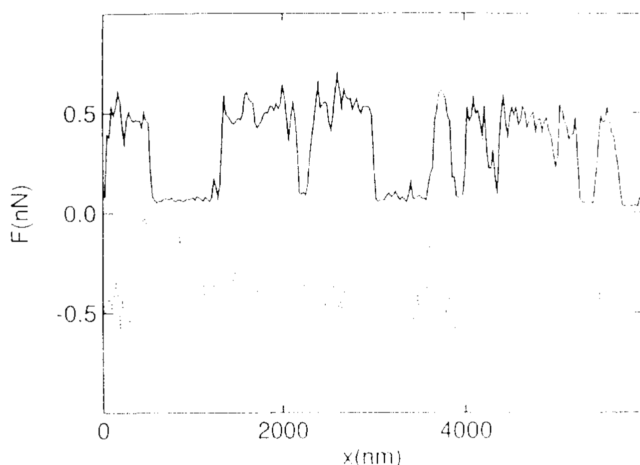

Figure 16: (a) Friction loop of a LB-monolayer prepared from a mixture of fluorocarbon and hydrocarbon carboxylates. The ratio between friction on fluorocarbon to hydrocarbon is 4 : 1 (from [101]).

The ability of FFM to give material-specific contrast is further demonstrated on mixed films of arachidic acid ($C_{19}H_{39}COOH$) and partially fluorinated carboxylic ether acid ($C_9F_{19}C_2H_4$-O-C_2H_4COOH) [100, 101]. The high circular domains shown in Fig. 15 are assigned to hydrocarbons while the surrounding flat regions are formed from fluorinated molecules. As represented by the friction loop in Fig. 16, the frictional forces on the fluorocarbons are about a factor of 4 larger than on the hydrocarbons. At first sight this observation is surprising. From the knowledge of compounds such as teflon (PTFE) a better tribological performance is expected for the fluorinated parts. Local scratch experiments have shown that the fluorocarbons are more robust than the hydrocarbons. Therefore, it is concluded that the fluorocarbons display good lubricating properties because they combine resistance to rupture with intermediate friction. Similar observations were previously made by SFA [102].

The above experiments demonstrate the potential of force microscopy in the field of tribology. Comparison of topography and friction force maps distinguishes between different materials and identifies local inhomogenieties. The combination with local scratch experiments and measurements of adhesion and elasticity may give further information to reveal the origins of friction and wear.

12 Elastic and Plastic Deformations

Similar to the concept of FFM, AFM measurements can be combined with elasticity measurements. The microscope can be operated either in the contact mode [103] or in the tunneling regime (with combined STM/AFM) [25] while the sample or tip is modulated with typically Å or tenths of Å and a few kHz. The modulated signal is fed into a lock-in amplifier and the output signal is proportional to the slope of the corresponding

force law, which is called local elasticity or local compliance. First experiments have demonstrated that the technique is able to find local impurities, such as hydrocarbons on gold [104]. Some theoretical investigations, where *ab initio* calculations were combined with continuum mechanics, have demonstrated that in the case of intercalated graphite, the concept of local elasticity is adequate even on an atomic scale [68, 105]. The authors predict that the elasticity measurements should distinguish between regions where the intercalated atoms sit in the first gallery (corresponding to reduced flexural rigidity) and regions where the intercalants are absent.

With higher repulsive contact forces, the sample or tip starts to deform plastically. For the Langmuir-Blodgett films mentioned above, the initial stages of wear are found already at low forces of 10^{-8}N [98]. First, small islands are removed in their entirety. Under these conditions the shear strength of the Langmuir-Blodgett films is determined by taking into account the area of the sheared island and the measured frictional force. Values of 1 ± 0.2MPa are found for Cd-arachidate films, in agreement with previous SFA-measurements. These experiments demonstrate that the instruments can also yield absolute numbers with reasonable accuracy. By further increasing the load and scan speed, layer-by-layer can be removed until the substrate is revealed [106, 81]. Systematic studies investigate inter- and intralayer interactions of these films. A ranking of interactions has been made for multilayers of Cd-arachidate, showing that the interaction between hydrophobic tails is weaker than the interaction between the hydrophylic heads. Furthermore, the interaction between tails of the first layer and the hydrophobized Si-substrate is found to be the strongest interaction [81]. On mixed films of hydrocarbons and fluorocarbons, it has been found that the hydrocarbons are more easily ruptured than the fluorocarbons [100].

A study of nanoindentations on LB-multilayers has been performed by Weihs et al. [107]. The authors determine Young's modulus, hardness and adhesion. An estimate of the contact diameter is provided by comparison with the Johnson-Kendall-Roberts-model. The authors expect that a minimum contact diameter of 2-3nm can be achieved due to plastic deformation which limits the resolution of AFM in the repulsive contact mode on these soft materials. The authors suggest that previous molecular resolution on LB-films [85, 76] is attributed to multiple tip imaging.

A systematic study of nanometer-scale scratching has been performed on polymers [108]. By increasing the force to 10^{-8}N and applying a modulation of a few kHz to the tip, a polycarbonate sample is patterned in a controlled way. On a compact disc a write density is demonstrated which is an order of magnitude better than the current technology. The displaced polymeric material is moved to the side and compressed. The scratch experiments are performed as a function of scan speed, sliding direction, modulation amplitude and static force. Afterwards, the surface is characterized with a lower, non-invasive force, where the fraction of elastic and plastic deformation can

be determined. Such experiments investigate plasticity on the nm-scale. By combining the AFM with a pulsed laser, very high write frequencies ($\approx$ kHz) have been achieved by Mamin et al. [109]. The laser is focused on the probing tip and locally melts the polymer. The basic limitation of the method is given only by the inertia of the cantilever. Again, further miniaturization could yield an improvement.

In the past few years, molecular dynamics calculations have become more sophisticated. Systems of up to a hundred thousand atoms and time scales in the nanosecond regime can already be treated. The empirical potentials become more and more complicated and include manybody terms. Examples are the Lennard-Jones [110], the standard two-body potential, Stillinger-Weber [111], which has a three-body term and is well-suited for silicon, and imbedded atom [112], which is dedicated to metals. The theoretical work is focussed on on metals. Nanoindentations are simulated, showing wetting and formation of a neck between a metallic tip (e.g. nickel) and a metallic sample (e.g. gold) [67]. Atoms move from the surface to the tip and vice versa. Experimental force vs. distance curves are compared with the simulated curves and agreement has been found.

In this context, the work of Dürig et al. has to be mentioned [16]. They use a different experimental approach to measure forces: a STM tip approaches a cantilever-type sample sensing forces between tip and sample. This work, performed in UHV, yields information about metallic adhesion and the transition to the point contact. Excellent agreement is found with quantum mechanical calculations where a universal relationship of the binding energy between metallic surfaces has been predicted [113]. At close separations, an avalanche of atoms from the metallic tip is expected [114]. Both experimental and theoretical work show that the transition to point contact with clean metallic tip and sample is a highly irreversible process.

A detailed investigation of the mechanisms of plastic deformations has been performed by Belak and coworkers, using molecular dynamics calculations [92]. They observe that a diamond tip on copper or silver does not produce dislocations. The metallic atoms are pushed into interstitial positions or are sheared to the side wall of the tip. These calculations have also demonstrated that for a nm-sized tip, the elastic strain distribution is in good agreement with the Hertzian theory.

13 Conclusions

A rich variety of forces can be sensed by force microscopy. In the non-contact mode, van der Waals forces produce images of topography whereas in the contact mode, ionic repulsion forces provide this information. Typical resolution of van der Waals imaging is 10nm. In the contact mode nm-resolution is common and can be improved down to the atomic scale under best conditions. Some restrictions have to be made for extremely

soft samples, such as biological materials, where elastic and plastic deformations often limit the resolution to tens of nm in the contact mode. In the non-contact mode, other forces, such as electrostatic forces from surface charges, magnetic forces from ferromagnetic domains, and capillary forces from thin liquid films can influence the contrast. Measurements in contact mode are less affected by these forces because the ionic repulsion forces increase steeply and can easily compensate the attractive forces without changing the z-position drastically (typically less than Å).

An understanding of the contrast mechanisms of contact AFM imaging on an atomic scale is still in its infancy. Simple hard sphere models give reasonable agreement to corrugation heights on ionic crystals. *Ab initio* calculations and molecular dynamics simulations yield upper limits of forces which a monatomic tip can withstand. The analysis of frictional forces has explained many of the phenomena of the original AFM work (large corrugation heights, distorted images..) but it has also raised a lot of fundamental questions about the origins of friction. Up to now, the phenomenon of *wearless* friction has been clearly demonstrated on an atomic scale. In some experiments on Langmuir-Blodgett films, material-specific contrast has been found. The method appears to be attractive because it goes beyond topography and finds local material inhomogenieties. In order to apply this method more routinely, it is necessary to ascertain the basic mechanisms of the dissipative processes.

With higher forces, plastic deformation is observed which gives some information about the initial stages of wear. Deformation mechanisms have been studied in great detail on metals. Significant material transport between tip and sample are calculated by molecular dynamics simulations. Therefore, clean metals appear to be rather unfavourable for imaging by contact AFM. However, experimental work in UHV is still rare and the first operational instruments are now being constructed.

AFM can be a useful tool in lithography. Nanometer-sized patterns can be scratched into polymers or Langmuir-Blodgett films. In combination with a pulsed laser, which melts the material around the tip, high rates of up to a few hundreds of kHz have been achieved.

The field of nanomechanics has already revealed some interesting, unexpected phenomena: e.g., observation of ultra-low friction coefficients on graphite and theoretical prediction of plastic deformation without generation of dislocations. Other investigations have demonstrated quite good agreement with classical models: e.g., elastic deformation at low forces, calculated with molecular dynamics, agrees well with Hertzian theory. Lubrication by thin films is also observed on the microscopic scale by FFM.

Experiments with electrostatic or magnetic forces have been found to be in agreement with classical theory. The resolution in these non-contact modes is typically 100nm and, under optimal conditions 10nm. These first experiments just demonstrated the capability of the microscopes and were dedicated to more applied questions, e.g., mag-

netic storage technology. However, some fundamental experiments have demonstrated the great potential of the technique: e.g. observation of single charge carriers or higher charge dissipation compared to macroscopic values. Finally, the regime of van der Waals forces offers a variety of unresolved questions: e.g. the theoretical prediction of van der Waals friction or the transition from the regime of retarded to non-retarded forces.

To conclude, with all the experimental and theoretical work we have just started to scratch and knock in a gentle way on the surface and now we are curious what comes out. Compared to the macroscopic world we expect to discover a rather different world, which is governed by different laws, the quantum mechanics. Many fundamental experiments on the nanometer scale are to be expected in the next years. Or to say it with the words of Richard Feynman: "There's plenty of room at the bottom" [115].

14 Acknowledgments

J. Frommer, R. Overney, L. Howald, R. Lüthi, H. Haefke, H.-J. Güntherodt and H. Rudin are acknowledged for stimulating discussions and excellent collaboration in the tribology group of the University of Basel. It is also a pleasure to thank O. Wolter, B. Terris, D. Rugar, M. Mate for providing illustrations. This work was supported by the Swiss National Science Foundation and the Komission zur Förderung der wissenschaftlichen Forschung. I would like to cite the outstanding contributions to the field of force microscopy of Dr. Martin Nonnenmacher who died under tragic circumstances in 1992. The scientific community lost with him a promising young scientist.

References

[1] G. Binnig and H. Rohrer, *Helv. Phys. Acta* **55**, 726 (1982).

[2] For a background see e.g. the proceedings of STM 91, *J. Vac. Sci. Technol. B* **9**, 401-1411 (1991). or STM 92 to appear in *Ultramicroscopy*, May (1992).

[3] G. Binnig, C.F. Quate and C. Gerber, *Phys. Rev. Lett.* **56**, 930 (1986).

[4] For earlier reviews see e.g.:
P.K. Hansma, V.B. Elings, O. Marti and C.E. Bracker, *Science* **242** 157 (1988).
H.K. Wickramasinghe, *Scientific American*, October (1989).
H. Heinzelmann, E. Meyer, H. Rudin and H.-J. Güntherodt, in *Scanning Tunneling Microscopy and Related Methods* R.J. Behm et al., eds., Kluwer Academic Publishers, (1990), p. 443.
D. Rugar and P. Hansma, Physics Today, October (1990).
E. Meyer and H. Heinzelmann, in *Scanning Tunneling Microscopy and Related*

Techniques R. Wiesendanger and H.-J. Güntherodt, eds., Springer Topics in Surface Science, Vol. 28, Springer Verlag, Berlin (1992), p. 99.
J. Frommer and E. Meyer, *J. Phys. Cond. Matt.* **S1**, 3 (1991).

[5] G. Binnig, Ch. Gerber, E. Stoll, T.R. Albrecht and C.F. Quate, *Europhys. Lett.* **3**, 1281 (1987).

[6] T.R. Albrecht and C.F. Quate, *J. Appl. Phys.* **62**, 2599 (1987).

[7] T.R. Albrecht, P. Grütter, D. Horne and D. Rugar, *J. Appl. Phys.* **69**, 668 (1991).

[8] K.L. Johnson, K. Kendall and A.D. Roberts, *Proc. Roy. Soc. London A* **324**, 301 (1971).

[9] J. Israelachvili, *Intermolecular and Surface Forces*, Academic Press, London, (Second Edition), (1992).

[10] J.B. Pethica and W.C. Oliver, *Physica Scripta* **T19**, 61 (1987).

[11] E. Meyer, H. Heinzelmann, P. Grütter, T. Jung, T. Weisskopf, H.-R. Hidber, R. Lapka, H. Rudin and H.-J. Güntherodt, *J. Microscopy* **151**, 269 (1988).

[12] O. Marti, B. Drake and P.K. Hansma, *Appl. Phys. Lett.* **51**, 484 (1987).

[13] P.J. Bryant, R.G. Miller and R. Yang, *Appl. Phys. Lett.* **52**, 2233 (1988).

[14] C.M. Mate, R. Erlandsson, G.M. McClelland and S. Chiang, *Surf. Sci.* **208**, 473 (1988).

[15] S. L. Tang, J. Bokor and R.H. Storz, *Appl. Phys. Lett.* **52**, 188 (1988).

[16] U. Dürig, J.K. Gimzewski and D.W. Pohl, *Phys. Rev. Lett.* **57**, 2403 (1986).
U. Dürig, O. Züger and D.W. Pohl, *Phys. Rev. Lett.* **65**, 349 (1990).

[17] M.D. Kirk, T.R. Albrecht and C.F. Quate, *Rev. Sci. Instrum.* **59**, 833 (1988).

[18] F.J. Giessibl and G. Binnig, *Ultramicroscopy* **42-44**, 281 (1992).

[19] G.M. McClelland, R. Erlandsson and S. Chiang, in *Review of Progress in Quantitative Non-Destructive Evaluation* **6B**, D.O. Thompson and D.E. Chimenti, eds., Plenum, New York (1987), p. 1307.

[20] R. Erlandsson, G.M. McClelland, C.M. Mate and S. Chiang, *J. Vac. Sci. Technol. A* **6**, 266 (1988).

[21] Y. Martin, C.C. Williams and H.K. Wickramasinghe, *J. Appl. Phys.* **61**, 4723 (1987).

[22] D. Rugar, H.J. Mamin and P. Güthner, *Appl. Phys. Lett.* **55**, 2588 (1989).

[23] D. Sarid, D.A. Iams, J.T. Ingle et al. , *J. Vac. Sci. Technol.* **A8**, 378 (1990).

[24] C. Schönenberger and S.F. Alvarado, *Rev. Sci. Instrum.* **60**, 3131 (1989).

[25] D. Anselmetti, C. Gerber, B. Michel, H.-J. Güntherodt and H. Rohrer, to appear in Rev. Sci. Instr. (1992).

[26] T. Oshio, N. Nakatani, Y. Sakai, N. Suzuki and T. Kataoka, *Ultramicroscopy* **42-44**, 310 (1992).

[27] G. Meyer and N. Amer, *Appl. Phys. Lett.* **53**, 1054 (1988).

[28] S. Alexander, L. Hellemans, O.Marti, J. Schneir, V. Elings, P.K. Hansma, M. Longmire and J. Gurley, *J. Appl. Phys.* **65**, 164 (1989).

[29] W.A. Ducker, R.F. Cook and D.R. Clarke, *J. Appl. Phys.* **67**, 4045 (1990).

[30] O. Marti, J. Colchero and J. Mlynek, *Nanotechnology* **1**, 141 (1990).

[31] G. Meyer and N.M. Amer, *Appl. Phys. Lett.* **57**, 2089 (1990).

[32] G. Neubauer, S.R. Cohen, G.M. McClelland, D. Horne, and C. M. Mate, *Rev. Sci. Instrum.* 61, 2296 (1990).

[33] T. Göddenhenrich, H. Lemke, U. Hartmann *J. Vac. Sci. Technol. A* **6**, 383 (1990).

[34] G.L. Miller, E.R: Wagner and T. Sleator, *Rev. Sci. Instrum.* **61**, 1267 (1990).

[35] O. Wolter, T. Bayer and J. Greschner, *J. Vac. Sci. Technol. B***9**, 1353 (1991).

[36] R.A. Buser, J. Brugger and N.F. de Rooij, *Ultramicroscopy* **42-44**, 1476 (1992).

[37] T.R. Albrecht and C.F. Quate, *J. Vac. Sci. Technol. A***6**, 271 (1988).
T.R. Albrecht, S. Akamine, T.E. Carver and C.F. Quate, *J. Vac. Sci. Technol. A*8, 3386 (1990).

[38] F. London, *Z. Phys.* **63**, 245 (1930).

[39] H.B.G. Casimir and D. Polder, *Phys. Rev.* **73**, 360 (1948).

[40] E.M. Lifshitz, *Zh. Eksp. Teor. Fiz.* **29**, 94 (1955). [*Soviet. Phys. JETP* **2**, 73 (1956).]

[41] U. Hartmann, *Phys. Rev. B* **42**, 1541 (1990).

[42] F.O. Goodman and N. Garcia, *Phys. Rev. B.* **43**, 4728 (1991).

[43] B.V. Derjaguin and I.I. Abrikosova, *Disc. Faraday Soc.* **18**, 33 (1954).

[44] D. Tabor, F.R.S. and R.H.S. Winterton, *Proc. Roy. Soc. A* **312**, 435 (1969).

[45] M. Nonnenmacher, J. Greschner and O. Wolter, *J. Vac. Sci Technol. B* **9**, 1358 (1991).

[46] Y.N. Moiseev, V.M. Mostepanenko, V.I. Panov and I.Y. Sokolov, *Phys. Lett. A* **132**, 354 (1988).

[47] J.B. Sokoloff, *Phys. Rev. B* **42**, 760 (1990).

[48] C. Schönenberger and S.F. Alvarado, *Phys. Rev. Lett.* **65**, 3162 (1990).

[49] J.E. Stern, B.D. Terris, H.J. Mamin and D. Rugar, *Appl. Phys. Lett.* **53**, 2717 (1988). D. Terris, J.E. Stern, D. Rugar and H.J. Mamin, *Phys. Rev. Lett.* **63**, 2669 (1989).

[50] B.D. Terris, J.E. Stern, D. Rugar and H.J. Mamin, *J. Vac. Sci. Technol. A* **8**, 374 (1990).

[51] F. Saurenbach and B.D. Terris, *Appl. Phys. Lett.* **56**, 1703 (1990).

[52] Y. Martin, D.W. Abraham, P.C.D. Hobbs and H.K. Wickramasinghe, *Electrochemical Soc. Proc. Mag. Mat. Process. Dev.* **90-8**, 115 (1989).

[53] P. Grütter, H.J. Mamin and D. Rugar, in *Scanning Tunneling Microscopy and Related Techniques* R. Wiesendanger and H.-J. Güntherodt, eds., Springer Topics in Surface Science, Springer Verlag, Berlin (1992), p. 151.

[54] C. Schönenberger and S.F. Alvarado, *Z. Phys. B* **80**, 373 (1990).

[55] D. Rugar, H.J. Mamin, P. Guethner, S.E. Lambert, J.E. Stern, I. McFadyen and T. Yogi, *J. Appl. Phys.* **68**, 1169 (1990).

[56] H.J. Hug, T. Jung, H.-J. Güntherodt and H. Thomas, *Physica C* **175** 357 (1991).

[57] A.L. Weisenhorn, P.K. Hansma, T.R. Albrecht and C.F. Quate, *Appl. Phys. Lett.* **54**, 2651 (1989).

[58] C.M. Mate, M.R. Lorenz and V.J. Novotny, *J. Chem. Phys.* **90**, 7550 (1989).

[59] C.M. Mate, M.R. Lorenz and V.J. Novotny, *IEEE Trans. Magn.* **26**, 1225 (1990).

[60] C.M. Mate and V.J. Novotny, *J. Chem. Phys.* **94**, 8420 (1991).

[61] N.A. Burnham, D.D. Dominguez, R.L. Mowery and R.J. Colton, *Phys. Rev. Lett.* **64**, 1931 (1990).

[62] G.S. Blackman, C.M. Mate and M.R. Philpott, *Phys. Rev. Lett.* **65**, 2270 (1990).

[63] I.P. Batra and S. Ciraci, *J. Vac. Sci. Technol. A* **6**, 313 (1988).

[64] W. Zhong, G. Overney and D. Tománek, *Europhys. Lett.* **15**, 49 (1991).

[65] U. Landman, W.D. Luedtke and A. Nitzan, *Surf. Sci.* **210**, L-177 (1989).
U. Landman, W.D. Luedtke and M.W. Ribarsky, *J. Vac. Sci. Technol. A* **7**, 2829 (1989).

[66] F. F. Abraham, I. P. Batra, and S. Ciraci. *Phys. Rev. Lett.* **60**, 1314 (1988).

[67] U. Landman, W.D. Luedtke, N.A. Burnham and R.J. Colton, *Science* **248**, 454 (1990).

[68] D. Tománek, G. Overney, H. Miyazaki, S.D. Mahanti and H.-J. Güntherodt, *Phys. Rev. Lett.* **63**, 876 (1989).

[69] W. Zhong and D. Tománek, *Phys. Rev. Lett.* **64**, 30 (1990).

[70] E. Meyer, D. Anselmetti, R. Wiesendanger, H.-J. Güntherodt, F. Lévy and H. Berger, *Europhys. Lett.* **9**, 695 (1990).

[71] R.D. Barrett, J. Nogami and C.F. Quate, *Appl. Phys. Lett.* **57**, 992 (1991).

[72] G. Meyer and N. Amer, *Appl. Phys. Lett.* **56**, 2100 (1990).

[73] E. Meyer, H. Heinzelmann, H. Rudin and H.-J. Güntherodt, *Z. Phys. B* **79**, 3 (1990).

[74] E. Meyer, H.-J. Güntherodt, H. Haefke and M. Krohn, *Europhys. Lett.* **15**, 319 (1991).
H. Haefke, E. Meyer, H.-J. Güntherodt, G. Gerth and M. Krohn, *J. Imag. Sci.* **35**, 290 (1991).

[75] E. Meyer, H. Heinzelmann, D. Brodbeck, G. Overney, R. Overney, L. Howald, H. Hug, T. Jung, H.-R. Hidber and H.-J. Güntherodt, *J. Vac. Sci. Technol. B* **9**, 1329 (1991).

[76] L. Bourdieu, P. Silberzan and D. Chatenay, *Phys. Rev. Lett.* **67**, 2029 (1991).

[77] T.R. Albrecht, M.M. Dovek, C.A. Lang, P. Grütter, C.F. Quate, S.W.J. Kuan, C.W. Frank and R.F.W. Pease, *J. Appl. Phys.* **64**, 1178 (1988).

[78] H. Haefke, E. Meyer, L. Howald, U. Schwarz, G. Gerth and M. Krohn, *Ultramicroscopy* **42-44**, 290 (1992).

[79] S. Blunier, H. Zogg, A.N. Tiwari, R.M. Overney, H.Haefke, P. Buffat and G. Kostorz, *Phys. Rev. Lett.* **68**, 3599 (1992).

[80] R.M. Overney, H. Haefke, E. Meyer and H.-J. Güntherodt, to appear in *Surf. Sci.* (1992).

[81] E. Meyer, L. Howald, R. Overney, D. Brodbeck, R. Lüthi, H. Haefke, J. Frommer and H.-J. Güntherodt, *Ultramicroscopy* **42-44**, 281 (1992).

[82] U. Schwarz, H. Haefke, Th. Jung, E. Meyer, H.-J. Güntherodt, R. Steiger and J. Bohonek, *Ultramicroscopy* **41**, 435 (1992).

[83] P. Grütter, W. Zimmermann-Edling and D. Brodbeck, *Appl. Phys. Lett.* **60**, 2741 (1992).

[84] V. Vogel and C. Wöll, *J. Chem. Phys.* **84**, 5200 (1986).

[85] E. Meyer, L. Howald, R.M. Overney, H. Heinzelmann, J. Frommer, H.-J. Güntherodt, T. Wagner, H. Schier, and S. Roth, *Nature* **349**, 398 (1991).

[86] R.M. Overney, E. Meyer, J. Frommer, G. Decher and J. Reibel, to appear in Langmuir (1992).

[87] O. Marti, H. Ribi, B. Drake, T. Albrecht, C. Quate and P. Hansma, *Science* **239**, 50 (1988).

[88] R.M. Overney, L. Howald, J. Frommer, E. Meyer, D. Brodbeck and H.-J. Güntherodt, *J. Chem. Phys.***94**, 8441 (1991).

[89] R.M. Overney, L. Howald, J. Frommer, E. Meyer, D. Brodbeck and H.-J. Güntherodt, *Ultramicroscopy* **42-44**, 983 (1992).

[90] A. Engel, *Ann. Rev. Biophys. Chem***20**, 79 (1991).
STM and SFM in Biology Ed.: O. Marti, Academic Press, London (1992).
W. Heckl, *Thin Solid Films* **207** (1992).

[91] G.M. McClelland, in *Adhesion and Friction* M. Grunze and H.J. Kreuzer, eds., Springer Series in Surface Sciences, Vol. **17**, Springer Verlag, Berlin (1989).

[92] J. Belak and I.F. Stowers, in *Fundamentals of Friction* I. Singer and H. Pollock, eds., Kluwer Academic Publisher (1992).

[93] R. Overney and E. Meyer (unpublished work).

[94] D. Tománek, W. Zhong and H. Thomas, *Europhys. Lett.* **15**, 887 (1991).

[95] C. M. Mate, G. M. McClelland, R. Erlandsson and S. Chiang, *Phys. Rev. Lett.* **59**, 1942 (1987).

[96] E. Meyer and H. Heinzelmann in *Scanning Tunneling Microscopy and Related Techniques* R. Wiesendanger and H.-J. Güntherodt, eds., Springer Topics in Surface Science, Springer Verlag, Berlin (1992), p. 99.

[97] T. Miyamoto, R. Kaneko and S. Miyake, *J. Vac. Sci. Technol.* **9**, 1336 (1991).

[98] E. Meyer, R. Overney, D. Brodbeck, L. Howald, R. Lüthi, J. Frommer and H.-J. Güntherodt, to appear Phys. Rev. Lett. (1992).

[99] E. Meyer, R. Overney, D. Brodbeck, L. Howald, R. Lüthi, J. Frommer and H.-J. Güntherodt, in *Fundamentals of Friction* I. Singer and H. Pollock, eds., Kluwer Academic Publisher (1992).

[100] R. Overney, E. Meyer, J. Frommer, D. Brodbeck, L. Howald, R. Lüthi, H.-J. Güntherodt, M. Fujihira, H. Takano and Y. Gotoh, *Nature* **359**, 133 (1992).

[101] E. Meyer, R. Overney, D. Brodbeck, L. Howald, R. Lüthi, J. Frommer, H.-J. Güntherodt, O. Wolter, M. Fujihira, H. Takano and Y. Gotoh, to appear in Thin Solid Films (1992).

[102] B.J. Briscoe and D.C.B. Evans, *Proc. Roy. Soc. A* **380**, 389 (1981).

[103] E.W. Stroup, A. Pungor, A.S. Lea, V. Hlady, J.D. Andrade, presented at the 203rd ACS National Meeting, San Francisco, April 5-10, (1992).

[104] D. Anselmetti (private communication).

[105] G. Overney, W. Zhong and D. Tománek, *J. Vac. Sci. Technol. B* **9**, 479 (1991).

[106] A.L. Weisenhorn, B. Drake, C.B. Prater, S.A.C. Gould and P.K. Hansma, *Biophys. J.* **58**, 1251 (1990).

[107] T.P. Weihs, Z. Nawaz, S.P. Jarvis and J.B. Pethica, (in press).

[108] T. Jung, H. Hug, A. Moser, U. Schwarz, D. Brodbeck and R. Hofer, *Ultramicroscopy* **42-44**, 1446 (1992).

[109] H.J. Mamin, H. Birk and D. Rugar, (in press).

[110] J.E. Lennard-Jones, *Trans. Faraday. Soc.* **28**, 334 (1932).

[111] F.H. Stillinger and T.A. Weber, *Phys. Rev. B* **31**, 5262 (1985).

[112] M.S. Daw and M.I. Baskes, *Phys. Rev. B* **29**, 6443 (1984).

[113] J.H. Rose, J.F. Smith and J. Ferrante, *Phys. Rev. B* **28**, 1835 (1983).

[114] J.R. Smith, G. Bozzolo, A. Banerjea and J. Ferrante, *Phys. Rev. Lett.* **63**, 1269 (1989).

[115] R.P. Feynman, *Engineering and Science* February, 22 (1960).